

Global Alignment of the CMS Muon System using a Track-Based Algorithm

Jim Pivarski, Alexei Safonov, Karoly Banicz, Riccardo Bellan

April 12, 2009

Abstract

It will have an abstract. Scope of the paper: baseline HIP procedure for barrel and endcap, CSC overlaps procedure for endcap. Methods described in full detail, results from a 50 pb^{-1} Monte Carlo study with the major systematic effects, results from CRAFT alignment (global muon only or global muon plus stand-alone? depends on time available), independent cross-checks, and $50\text{--}200 \text{ pb}^{-1}$ prediction for muon momentum resolution. It will back up a much shorter public paper. Completed in this version: everything except results and conclusions (sections 4, 5, and 7).

Contents

1	Introduction	3
1.1	Geometry of the muon system	4
2	Description of the global alignment algorithm	6
2.1	Alignment datasets and track-fitting procedures	8
2.2	Calculation of super-residuals	9
2.3	Fitting the super-residuals distribution	11
2.4	Determining alignment parameters from fits	13
2.5	Accommodating errors in magnetic field and material budget	17
3	Monitoring Tools and Validation/Verification	21
3.1	Comparison of geometries in the database	22
3.2	Validating residuals fits	22
3.3	Muon system maps	23
3.4	Verification with relative residuals	26
4	Global alignment results with collisions Monte Carlo	28
4.1	Scaling with statistics	28
4.2	Dependence on tracker misalignment	28
4.3	Dependence on magnetic field errors	28
5	Global alignment results with cosmic ray data	28
5.1	Validation plots	28
5.2	Verification with relative residuals	28
5.3	Verification with stand-alone muon alignments	28
5.4	Verification with cosmic track splitting	28
6	Relative alignment of CSCs with local tracks	28
6.1	Description of the CSC Overlaps algorithm	29
6.2	Local CSC alignment parameters	31
6.3	Specialized trigger and data streams	32
6.4	Results from the 2008 LHC run	33
6.5	Extension to align CSC layers	36
6.6	Verifying the global procedure with local alignment	37
7	Alignment outlook for 2009–2010	39

1 Introduction

The CMS experiment features a large muon tracking system which will likely be essential for early LHC discoveries. As with all tracking systems, the resolution of its reconstructed tracks depends on two main components:

- intrinsic hit resolution, or how precisely the intersection of passing particles with its measurement planes can be determined for individual tracks, and
- alignment, or how accurately the position of the measurement planes are known in 3-D space, affecting all tracks.

These components combine in quadrature, so track resolution can be expected to improve significantly until the alignment is much better than the intrinsic resolution, which is about 200–300 μm for the CMS muon system. Therefore, our baseline goal for the 2009–2010 physics run is to align the muon system to this level of accuracy.

Though this 44-layer muon system can act as a tracking system on its own, it was designed to operate in conjunction with the other CMS subsystems, particularly the inner silicon tracker. Together, the two tracking subsystems form a global tracking system with high intrinsic hit resolution in the tracker and large lever arm in the muon system (particularly important for high- p_T tracks; $1/p_T$ resolution scales with lever arm squared). Above $p_T \gtrsim 200$ GeV in the barrel and 1 TeV in the endcap, the inclusion of muon system hits significantly improves muon resolution over a tracker-only measurement (Fig 1). Muon alignment is therefore important for any physics analysis featuring high- p_T muons, such as $Z' \rightarrow \mu\mu$ and $W' \rightarrow \mu\nu$, but it is also important for analyses that use the muon system as an independent check on the tracker, such as the search for heavy stable charged particles, which verifies velocity from tracker dE/dx with muon barrel timing (equivalent to spatial resolution).

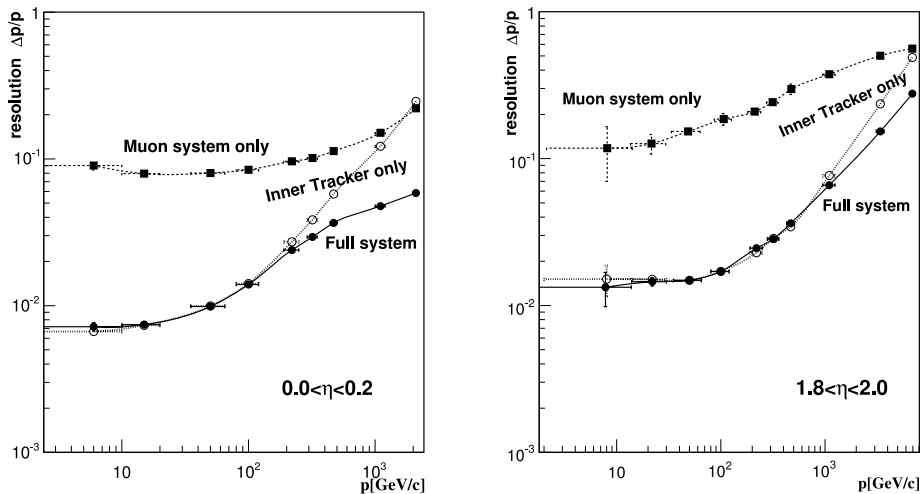


Figure 1: Momentum resolution of the inner tracker, muon system, and combined system, as a function of p_T and η . (Source: Physics TDR [1])

To obtain high-quality global muon tracks, the tracker and muon system must be aligned in the same coordinate system. We choose to define the global coordinate system as the inner tracker’s system and verify that it is stable for each block of runs. This is convenient because the low-momentum tracks used to measure the alignment (20–100 GeV) are best determined by the tracker. If a sudden movement or slow drift is observed, we have the necessary machinery to redefine the global coordinate system in a more neutral way.

There are several independent ways to measure alignment, all of which are actively being pursued. Alignment with global tracks provides a simple way to link distant subdetector elements and is sensitive to exactly the same parameters as the final physics object: the global muon itself. For example, if misalignment perpendicular to the measurement plane of a layer cannot be determined from a large sample of tracks, then it also does not distort the physics resolution of muons in the same sized sample. Alignment with local tracks, such as linear track stubs through pairs of neighboring detector elements, can determine the relative positions of those elements and provide both an early (low statistics) alignment measurement and a powerful cross-check on the global alignment, as local tracks are much less sensitive to propagation errors and can correlate measurements in different combinations than the global method. The CMS muon system is also instrumented with a network of physical measurement devices such as lasers, calipers, and inclinometers, which provide another independent measurement of detector alignment, free from any tracking errors but requiring a careful propagation of cumulative measurements. This paper will focus on alignment with global tracks for both the barrel and the endcap, and demonstrate an alignment procedure with local tracks in the endcap.

1.1 Geometry of the muon system

The muon system contains three basic types of tracking chambers: drift tube (DT) chambers in the barrel, cathode strip chambers (CSC) in the endcap, and resistive plate chambers (RPC) in both. The chambers are modular tracking detectors, 1–4 m each, whose internal geometry is well understood from production tests. They are mounted on 15 m tall barrel wheels and endcap disks which serve to compactly return the solenoid’s magnetic field and also filter all particles except for muons. The position and orientation of each chamber is allowed to slip under the influence of the 3.8 T CMS solenoid, rather than distort the chambers non-rigidly. In the center of the endcap, the distortion can be as large as 1.4 cm.

This paper focuses on algorithms to align the DT chambers and CSCs as rigid bodies whose internal geometry is assumed to be known. The DT internal geometry has been thoroughly studied elsewhere [2], and a method to align CSC layers will be described in section 6.5. The RPCs are used primarily for triggering with a resolution of 1–2 cm, so they don’t contribute to muon resolution and don’t need to be aligned.

The chambers are grouped in stations (loosely by distance from the interaction point), wheels/disks (modular transverse slices), and sectors/chambers (azimuthal divisions). Table 1 presents an overview of this structure, and Fig 2 shows where the stations are located in CMS.

In barrel stations 1–3, DT chambers contain superlayers which measure orthogonal directions: superlayers 1 and 3 measure the muon distance of closest approach in the transverse plane, while superlayer 2 measures the longitudinal closest approach, parallel with the beam-

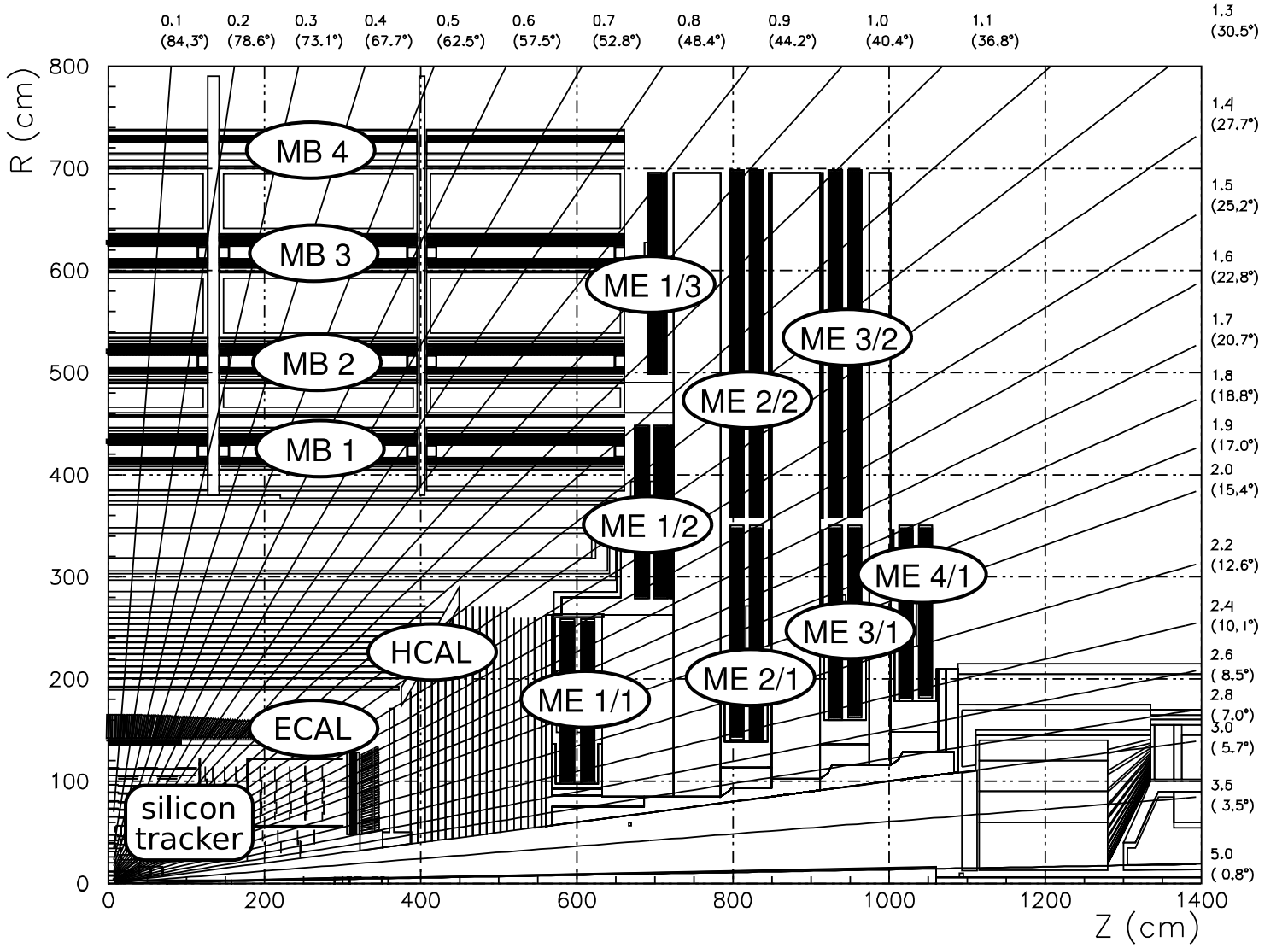


Figure 2: A quarter-view of CMS with labeled muon barrel (MB) and endcap (ME) stations.

Table 1: Geographical organization of muon chambers.

Barrel			Endcap		
wheels	-2 to +2	physically moveable transverse slices	endcaps	- and +	forward and backward halves
stations	MB1 to 4	cylinders of fixed radius from beam-line	disks	ME1 to 4	physically moveable transverse slices
sectors	1-12 (1-14 in station 4)	$\phi = 0$ is sector 1, increasing counter-clockwise	rings (stations)	1/1ab, 1/2, 1/3, 2/1, 2/2, 3/1, 3/2, 4/1	rings of fixed radius from beamline
			chambers	1-36 (1-18 in 2/1, 3/1, 4/1)	$\phi = 0$ is sector 1, increasing counter-clockwise

line. Barrel station 4 chambers have no superlayer 2, so they are one-dimensional devices. Each chamber has a local coordinate system, where local x is the coordinate superlayers 1 and 3 measure, local y is the coordinate superlayer 2 measures, and local z is orthogonal to the measurement plane. By contrast, the global x coordinate is the horizontal distance from the beamline, global y is vertical, and global z is parallel to the beamline, roughly coinciding with the DT local y . The goal of alignment can be restated as a very careful determination of the transformation functions between the local coordinate systems and the global system.

In the CSCs, cathode strips fan radially from the beamline, intersected by anode wires. We define the same sort of local coordinate system in the CSCs, with local x being the direction measured mostly by strips, local y as the direction measured by wires, and local z perpendicular to the measurement plane, roughly corresponding with global z . Table 2 summarizes the coordinate systems.

2 Description of the global alignment algorithm

The basic idea is to accumulate high- p_T muons which pass through two regions: a well-aligned reference volume, usually the silicon tracker, and the target volume under study. Muon tracks are fitted using information from the reference only, and alignables in the target (muon chambers, layers, wheels, or disks) are translated and rotated to minimize the difference between muon tracks and muon hits (residuals).

This procedure can be seen as an extreme limit of the HIP algorithm used to align the silicon tracker, in which tracks are fitted in a single tracking volume with large uncertainties

Table 2: Definitions and correspondance of coordinate systems.

Global frame		Local DT frames		Local CSC frames	
x	horizontal, toward center of LHC	x	superlayer 1 and 3 measurement, roughly global $r\phi$	x	strip measurement, roughly global $r\phi$
y	vertical, up				
z	along beamline	y	superlayer 2 measurement, roughly global z	y	wire measurement, roughly radial from beamline
origin	nominal interaction point				
$r\phi$	combination of x and y perpendicular to rays from the beamline	z	out of plane, roughly radial from beamline	z	out of plane, roughly global z
		origin	center of chamber	origin	center of chamber

ϕ_x , ϕ_y , and ϕ_z are rotation angles around local coordinate axes.

in the positions of the alignables, which reduces the sensitivity of the final track fits to outlying alignables. Outlying alignables tend to have larger residuals, which are used to pull them toward their rightful positions with repeated applications of the procedure.

In comparison with the silicon tracker alignment case, however, individual tracks propagated through the muon system are much less trustworthy due to the large amounts of material they must penetrate. Muons, particularly low-momentum muons, can be highly deflected by the single and multiple scattering which occurs unpredictably in dense material, and can distort the track-fit if not recognized by the algorithm. Since our track-fitting algorithm properly includes such scattering, a direct application of the tracker alignment procedure would lead to overzealous application of scattering by the track-fitting algorithm: the displacement of muon hits in misaligned chambers would be overcorrected by a scattering assumption, and thus adversely affect all or most of the tracks in the sample. By freely propagating muon tracks from the reference volume through the target volume, and not allowing the muon hits to bias the propagated track, only the muons that actually do scatter significantly are useless for alignment.

The technique is particularly useful when the reference volume is the silicon tracker, since the tracker dominates the precision of track parameters for the muons used in alignment ($20 < p_T < 100$ GeV). The disadvantage is that any distortions in the tracker geometry, which can persist after completing tracker alignment if the χ^2 of its tracks are invariant under such transformations, would be extrapolated to the muon system, distorting the muon geometry in the same way. However, the broad track angle distribution of cosmic rays allows us to observe residuals on tracks from different parts of the reference volume, and therefore put bounds on the bias from the track source. The tracker alignment procedure uses this same technique to constrain its “weak modes,” but the muon system provides additional checks with a longer lever arm, to amplify the errors and more easily notice the effects.

It's also a computationally useful feature that excluding target hits from the track-fit eliminates the coupling between track-fitting and alignment. We therefore do not need to iterate the procedure, as in the case in the tracker-HIP alignment, because geometry updates in the target have no effect on track-fitting in the reference. In the language of MillePede-based algorithms, the matrix of alignment parameters and track parameters becomes block-diagonal, greatly simplifying its inversion and eliminating the fundamental distinction between the HIP and MillePede approaches.

2.1 Alignment datasets and track-fitting procedures

Data for muon HIP alignment are derived from three main sources: LHC collisions, cosmic rays that pass through the tracker, and all cosmic rays (relaxing tracker-pointing increases the sample by an order of magnitude). The main difference is in their orientations: collisions muons originate strictly in the interaction point at the center of CMS and are nearly symmetric in ϕ and charge, while cosmic rays are more broadly distributed in entrance angles, though steeply peaked toward the vertical, with 30% more μ^+ than μ^- . It should be noted that all collisions muons which reach a given chamber pass through approximately the same region of the tracker, and can therefore be sensitive to local errors in the tracker alignment, while cosmic rays are only sensitive to global distortions in the tracker. The distinction between tracker-pointing and non-tracker-pointing cosmic rays is important because only the former can use the tracker as a reference.

The production mechanism of collisions muons doesn't need to be controlled, only the p_T distribution. Whether a muon was the product of a b decay or a Z decay, its propagation through the tracker and muon system is determined solely by its momentum. (A future incarnation of this algorithm may take advantage of the mass constraint from a large Z , Υ , or $J/\psi \rightarrow \mu\mu$ sample to reduce reference bias, but this version doesn't.) The influence of muons from pions decaying in flight is minimized in the same way as highly scattered muons, which will be described in section 2.3. We therefore only require one muon in the event, with $20 \text{ GeV} < p_T < 100 \text{ GeV}$. The lower limit excludes tracks that are likely to scatter and the upper limit guarantees that track parameters are well determined by the tracker. This distribution is highly peaked at the low momentum end of the spectrum, as it is dominated by QCD-related sources.

The events are collected by AlCaReco producers, which select good muons in prompt reconstruction at CERN's Tier-0, reduce the data streams to include only the needed tracks and hits, and send them to the CMS CAF to be persistently stored on a local disk. The AlCaReco stream for collisions muons is named MuAlCallIsolatedMu (though no isolation requirements are applied), the stream for tracker-pointing cosmics is MuAlGlobalCosmics, and the stream for all cosmic rays is MuAlStandAloneCosmics.

The first step in the alignment algorithm is to re-fit the tracks, using the original track parameters to seed the new fit. This allows us to take advantage of any updates in the tracker geometry and to fit global-muon tracks with artificially large errors in the muon alignable positions. (Global muon tracks each contain a list of associated hits from both the tracker and the muon chambers, and have passed standard quality requirements for matching the tracker and muon stubs to each other.) By imposing artificially large errors on the muon hits (a variance of 1000 cm^2 , isotropically in x - y - z), the new track fit effectively

ignores them, giving us the desired tracker-only fit with the muon residuals calculated by the same subroutines as standard track-reconstruction, to be certain that we’re optimizing the same quantity that will be used to fit tracks. When aligning with stand-alone muons (which have no tracker hits), we define the reference and target volumes by setting large errors to selected chambers. These errors are expressed in a mutable database record, so the boundary between reference and target can be arbitrarily defined.

In performing the re-fit, it is essential that the algorithm starts with the reference hits and ends with the target hits; otherwise, the new track’s trajectory through the target will be determined by the old seed track, rather than a new fit to the reference. For collisions muons, this means that fitting must be performed in the direction of the muon momentum (“alongMomentum” or “insideOut”), and for cosmic rays, two specialized refitters, `globalCosmicMuonTrajectories` and `standAloneMuonTrajectories`, have been written to set the hit order in a reliable way. The `globalCosmicMuonTrajectories` algorithm arranges hits to start in the tracker and end in the muon system, while `standAloneMuonTrajectories` requires the first hit to be the closest to the center of the detector, so that alignment knowledge can be propagated from wheel 0 out to the endcaps.

2.2 Calculation of super-residuals

As a tracking volume, the muon system is highly structured. Inside of each chamber, muons encounter very little material, and in the barrel chambers, very little magnetic field. Muon hits are therefore more highly correlated with their neighbors in the same chamber than they are with propagated tracks.

If we ignore this fact, we would misrepresent the statistical resolution of the alignment result. For the sake of argument, consider an extreme case in which residuals in an N -layer chamber are 100% correlated with each other. If we accumulate a histogram of residuals for that chamber, each track will yield the same result N times, though the distribution would be wide because of uncertainties in track propagation. If we then compute the mean of that distribution or fit it, the reported uncertainties would be a factor of \sqrt{N} too small.

Instead, we combine all residuals on one track in one chamber into a single super-residual; each super-residual is an independent measurement. We compute a super-residual from the constant term in a linear fit of residuals Δx_i as a function of local z , the coordinate perpendicular to the chamber’s layer planes. Non-zero slopes in $\Delta x(z)$ are either caused by errors in the track’s local trajectory or by rotations of the chamber (around $z = 0$). The constant term from this fitting method is more representative of the chamber’s overall residual than a mean of Δx_i would be, because the hits are not necessarily symmetric around the chamber center in z , especially if hit inefficiencies or weighting are allowed (see Fig 3). The linear fit is computed analytically, with weights from intrinsic hit uncertainties (σ_i).

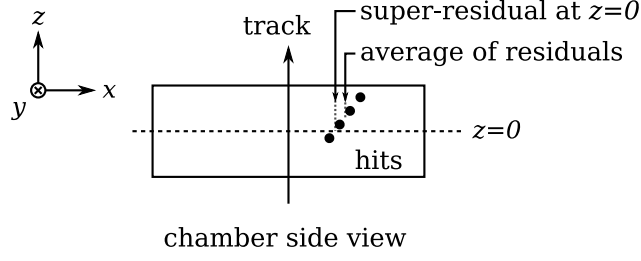


Figure 3: A super-residual is the constant from a linear fit to residuals vs. local z , and is therefore a better measure of the “residual at chamber center” than the average of residuals.

$$\text{constant} = \frac{1}{\text{denominator}} \left(\sum \frac{z_i^2}{\sigma_i^2} \sum \frac{\Delta x_i}{\sigma_i^2} - \sum \frac{z_i}{\sigma_i^2} \sum \frac{z_i \Delta x_i}{\sigma_i^2} \right) \quad (1)$$

$$\text{slope} = \frac{1}{\text{denominator}} \left(\sum \frac{1}{\sigma_i^2} \sum \frac{z_i \Delta x_i}{\sigma_i^2} - \sum \frac{z_i}{\sigma_i^2} \sum \frac{\Delta x_i}{\sigma_i^2} \right) \quad (2)$$

$$\text{where denominator} = \sum \frac{1}{\sigma_i^2} \sum \frac{z_i^2}{\sigma_i^2} - \left(\sum \frac{z_i}{\sigma_i^2} \right)^2 \quad (3)$$

Barrel DT chambers measure two coordinates, local x and y , but with disjoint sets of hits. Hits in superlayers 1 and 3 measure the local x coordinate (approximately global $r\phi$) but not y , while hits in superlayer 2 measure local y (parallel with the beamline) but not x . We therefore treat these as two independent systems and compute one super-residual for superlayers 1 and 3 and another super-residual for superlayer 2.

Endcap CSCs also measure two coordinates using different systems— cathode strips and anode wires— though they do not decompose into an orthogonal, rectilinear coordinate system. Strips measure $r\phi$, the curvilinear coordinate which is always perpendicular to rays from the beamline, while wires measure y or a linear combination of x and y , depending on the station. The wire measurement is not useful for alignment because its granularity is much larger than the alignment precision, ?? to 5 cm. (One could use edges in hit efficiency to determine y , but that’s beyond the scope of this paper.) Using only strips, it is most convenient to compute $r\phi$ super-residuals and apply alignment corrections in $r\phi$, rather than the CSCs’ local x coordinates (Fig 4). Other than its interpretation, CSC $r\phi$ super-residuals are treated the same way as DT x super-residuals in alignment fits.

By combining hit information into one or two measurements per chamber, super-residuals are similar to, but not exactly the same as 2-D segment residuals, the distance and angular difference between a track and a linear fit to the hits in the chamber. The distinction is that segment residuals assume that the muon’s propagation through the chamber is linear, while super-residuals only assume that the growth of error between the true and reconstructed paths is linear. The actual path of a muon may be significantly non-linear in ME1/1 and ME1/2, which contain 2.5 T and 1.0 T fields inside the gas volumes, respectively. Super-residuals represent deviations in these chambers with more precision than a segment residual would.

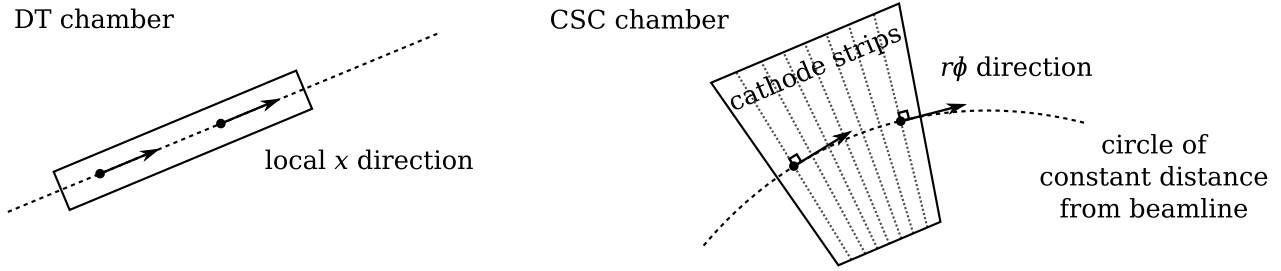


Figure 4: Local x and y coordinates in DT chambers are rectilinear, but the fanning of CSC strips makes it more convenient to measure residuals and align CSCs in curvilinear $r\phi$.

2.3 Fitting the super-residuals distribution

Once a large set of super-residuals has been collected for each chamber, its alignment correction is computed from the mode of its distribution. The mode is to be preferred over the mean and the median because the alignment signal has a background which is not guaranteed to be symmetric.

Each super-residual can be thought of as a single track's notion of where the chamber is, and the combined measurement should be determined from the most popular answer. Muons that scatter or are misrepresentative because they're actually from pion decays-in-flight divide their votes among a continuum of wrong answers, while good muons with minimal scattering agree on a single answer, with some Gaussian smearing. The distribution of residuals from scattering depends on the distribution of material in front of the chamber and the angles of the tracks used for alignment, which need not be symmetric at a given point in the detector. This asymmetry would skew an average of the super-residuals distribution, but it has much less impact on the peak position.

To determine the mode of a distribution from a random sample, one must fit it with an ansatz of known mode. The physical scattering processes generally have power-law distributions and the extrapolation of a trajectory from experimental measurements smears the peak of nearly zero scattering into a Gaussian bell-curve (see Fig 5). These effects are best represented by a convolution:

$$f(\Delta x; x_0, \sigma, \Gamma) = \int_{-\infty}^{\infty} \frac{1}{\pi} \frac{\Gamma/2}{(\Delta x - \xi - x_0)^2 + (\Gamma/2)^2} \times \frac{1}{\sqrt{2\pi}\sigma} \exp\left(\frac{-\xi^2}{2\sigma^2}\right) d\xi \quad (4)$$

where x_0 is the mode of the residuals $\{\Delta x_i\}$, σ is the experimental resolution and Γ is the full width at half maximum of a Cauchy-Lorentz distribution, chosen for its power-law tails and simplicity. This ansatz does not describe the scattering background in detail, as the real distribution might scale with a different power and the Cauchy-Lorentz distribution isn't asymmetric, but it absorbs much of the background and allows the Gaussian part to more accurately fit the peak (see Fig 6).

We fit Eqn 4 to the super-residuals of each chamber with an unbinned maximum likelihood method to handle low-statistics cases well and to avoid dependence on bin width. It should be noted that a simple average ($\sum \Delta x_i / N$) is equal to the mode of an unbinned Gaussian fit, so while this algorithm may be procedurally much more complicated, it is functionally

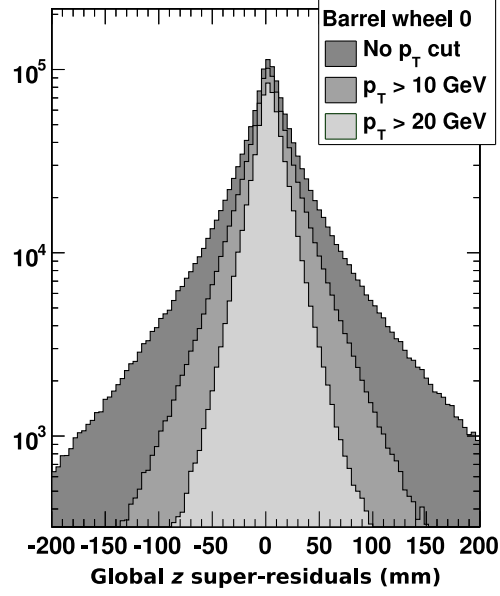


Figure 5: Super-residuals distributions have a central Gaussian core from unscattered muons and power-law tails from scattered muons. This is demonstrated by taking advantage of the fact that scattering is highly correlated with p_T .

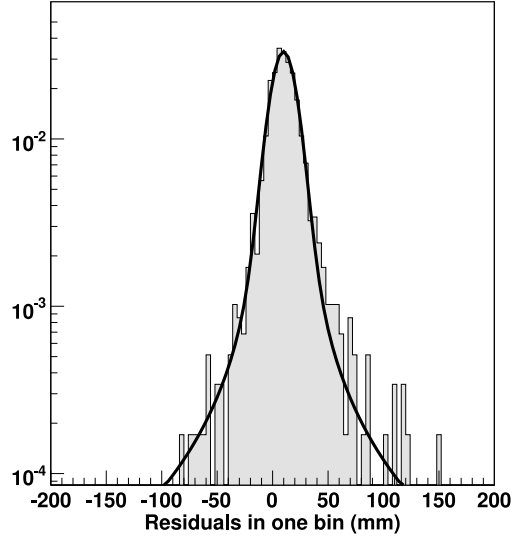


Figure 6: Fit function for residuals with a Gaussian core and power-law tails. The residuals in this plot were selected from a geographically small region of the detector (within DT station 4, wheel 0) to avoid smearing from misalignment, and the fit was performed without binning.

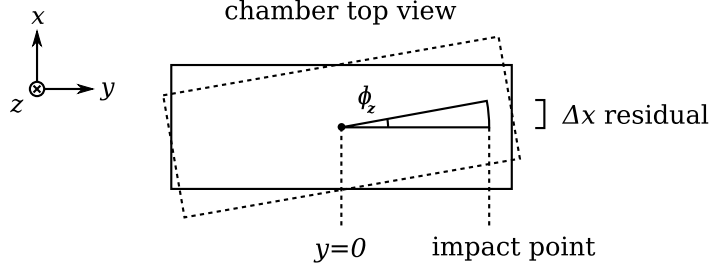


Figure 7: If the chamber is rotated in its layer plane (ϕ_z misalignment), the crest of the Δx residuals distribution will vary with y impact point as $\Delta x = \sin \phi_z \cdot y$ or $\Delta x \approx \phi_z y$. We include ϕ_z as a free parameter in the fit to perform this alignment, simultaneously with δx . The same holds for Δy residuals and the x impact point.

a small modification from just using the mean. Outlying residuals contribute much less to the log-likelihood of f than they would to the log-likelihood of a Gaussian tail, and hence they have much less influence on the fitted value of x_0 , regardless of whether they're symmetrically distributed or not. We also reject any residual beyond 10 meters of zero or 10 standard deviations of the mean for robustness against nonsense input.

For computational efficiency, Eqn 4 is pre-computed in bins of σ and Γ . Bilinear interpolations from the look-up table have been verified up to $|\Delta x| < 100 \sigma$ and $\Gamma < 10 \sigma$. If the MINUIT fit settles upon a value outside of this table, it is treated as a fit failure.

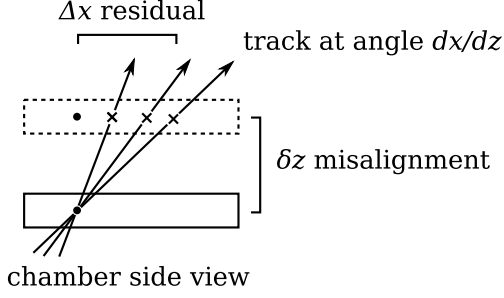
This procedure was developed to manage asymmetric residuals from scattering. The CMSSW track propagator computes appropriate error ellipses for multiple scattering when it propagates through dense material, but our method of de-weighting hits in the target volume by inflating chamber position uncertainties washes out that information, so we won't be able to use it the way the tracker HIP algorithm does. Also, if we were to rely on the propagator's estimate of scattering, rather than fitting it in the data, our algorithm would depend on the track reconstruction's assumed material budget, which might be wrong.

2.4 Determining alignment parameters from fits

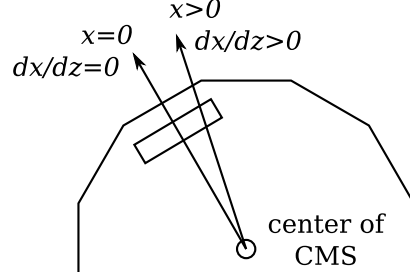
We collect x and y super-residuals from each DT chamber and $r\phi$ super-residuals from each CSC, so determining only the peak of each distribution would only allow us to align DT chambers in two dimensions and CSCs in one. We want to align as many of the 6 rigid body degrees of freedom as possible, and fortunately, we can access most of the others by identifying trends in the residuals distributions.

Consider a chamber rotated around its local z axis, as shown in Fig 7. This ϕ_z rotation creates discrepancies between tracks and their hits at the edges of the detector, but not in the center. For small misalignments ($\sin \phi_z \approx \phi_z$), the Δx residual is proportional to the y position of the impact point, and the Δy residual is proportional to the x position of the impact point, with the constant of proportionality in both cases being ϕ_z .

We can extract δx and ϕ_z alignment corrections from a collection of superlayer 1 and 3 super-residuals by fitting the distribution to a straight line; a fit to δy and ϕ_z in the superlayer 2 super-residuals allows us to cross-check ϕ_z from an independent dataset. A



(a) Linear relationship between Δx residuals, δz misalignment, and dx/dz track angle:
 $\Delta x = (dx/dz) \delta z$



(b) Correlation between x impact point and dx/dz track angle for tracks that pass close to the origin

Figure 8: Misalignments perpendicular to the measurement plane (local z) are included in the fit as a linear trend with respect to track entrance angle (which is often correlated with impact point). The same holds for Δy residuals and the dy/dz track entrance angle.

discrepancy between the two ϕ_z fits would indicate a problem with the chamber geometry description. In a future version of the algorithm, when this validity has been fully established, we can use the higher-precision superlayer 1 and 3 ϕ_z result to improve the accuracy of superlayer 2 fits for δy . It is important for the fits to either know the correct ϕ_z value or fit for it, because an incorrect ϕ_z would bias δx or δy if the distribution of muons across the surface of the chamber is asymmetric.

Linear fits are included in the residuals fit described in section 2.3 by expanding the x_0 parameter (Eqn 4) into an expression involving two parameters. To determine δ_x and ϕ_z alignment corrections, we expand f to

$$f_x(\Delta x, y_{\text{impact}}; \delta_x, \phi_z, \sigma, \Gamma) \text{ with } (\delta_x + y_{\text{impact}} \phi_z) \text{ replacing } x_0 \quad (5)$$

and for δ_y and δ_{ϕ_z} , we use

$$f_y(\Delta y, x_{\text{impact}}; \delta_y, \phi_z, \sigma, \Gamma) \text{ with } (\delta_y + x_{\text{impact}} \phi_z) \text{ replacing } x_0. \quad (6)$$

In both cases, the impact point is taken from the track extrapolation, rather than the hits themselves. (Not all chambers have enough information to determine the impact point in both dimensions, and it doesn't need to be known with high precision.)

Next, consider a chamber which has been misaligned in the local z direction, as shown in Fig 8(a). The offset introduces Δx and Δy residuals for angled tracks, proportional to the dx/dz and dy/dz angles, respectively. We can compute the δz alignment correction by adding this dependence to the fit as well.

$$f_{xz}(\Delta x, y_{\text{impact}}, \frac{dx}{dz}; \delta_x, \phi_z, \delta_z, \sigma, \Gamma) \text{ with } x_0 \rightarrow (\delta_x + y_{\text{impact}} \phi_z + \frac{dx}{dz} \delta_z) \quad (7)$$

$$f_{yz}(\Delta y, x_{\text{impact}}, \frac{dy}{dz}; \delta_y, \phi_z, \delta_z, \sigma, \Gamma) \text{ with } x_0 \rightarrow (\delta_y + x_{\text{impact}} \phi_z + \frac{dy}{dz} \delta_z) \quad (8)$$

In the superlayer 2 case, however, the distribution of muon $\frac{dy}{dz}$ entrance angles is highly asymmetric, which would make Eqn 8 a long-baseline extrapolation. We therefore only

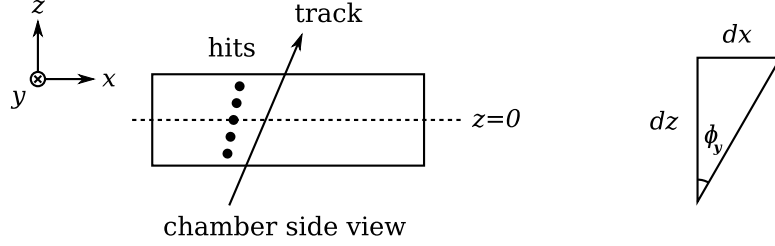


Figure 9: Super-residuals have both a value at the chamber center and a slope. The dx/dz slopes are used to align ϕ_y and the dy/dz slopes (where available) align ϕ_x .

fit for δ_z in superlayer 1&3 and the CSCs, and in a future version of the algorithm, the superlayer 1&3 result would be used to improve superlayer 2 accuracy.

To measure ϕ_z , we had to look at Δx residuals as a function of y_{impact} , and to measure δz , we had to look at the same residuals as a function of dx/dz . Note that dx/dz is correlated with x_{impact} (Fig 8(b)), especially for muons from the collision point. (Similarly for Δy , x_{impact} , and y_{impact} .) If we think of dx/dz as being equivalent to x_{impact} , we have used all of the spatial information available to us, and have only determined δ_x , δ_y , δ_z (two ways), and ϕ_z (two ways).

To get the ϕ_x and ϕ_y angles, we go back to the super-residuals and note that the slope of the linear fit to individual hit residuals versus z yields a difference in angle between the track and the hits. As can be seen in Fig 9, the dx/dz slope of a super-residual is $\tan \phi_y$, where ϕ_y is the angle between the track's direction and the direction suggested by the hits. Approximating these as small angles, we take the super-residual dx/dz slopes to be ϕ_y residuals and dy/dz slopes to be ϕ_x residuals, and fit them to Eqn 4.

It is necessary to control the ϕ_x and ϕ_y alignment corrections for impact point, or else ϕ_z misalignments will appear as spurious ϕ_x and ϕ_y corrections when the track source is asymmetric in entrance angle and position. This is a fully 3-dimensional effect, diagrammed as well as possible in Fig 10. To account for this, we add x and y impact point corrections to the fit function, analogous to Eqns 5-8.

The fact that scattering occurs in localized regions of the detector introduces a strong correlation between super-residual positions and their angles, illustrated in Fig 11. Disagreement between a track's direction and the direction suggested by its hits is a good indication that the muon has been scattered. We take advantage of this relationship to improve precision in the δx and δy measurements in three ways:

- include the average Δx vs. ϕ_y and Δy vs. ϕ_x trends as slope parameters in the fits,
- select only super-residuals that have slopes in a well-behaved linear region around zero (5 mrad in superlayer 1&3 and CSCs, 30 mrad in superlayer 2), and
- use the measured ϕ_y or ϕ_x alignment to correct δ_x and δ_y , respectively.

Depending on the location of the chamber, accounting for this correlation improves the fitted precision by as much as a factor of 2. The algorithm can be improved further by identifying and correcting any other large correlations in the shape of the residuals distributions:

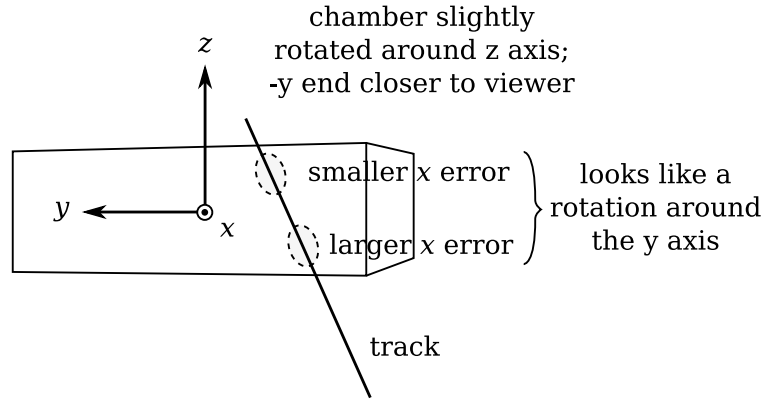


Figure 10: A 3-dimensional effect in which ϕ_z misalignments can masquerade as ϕ_y misalignments when the track source is asymmetric in dx/dz entrance angle and y impact point. The same is true for ϕ_x misalignments, swapping all $x \leftrightarrow y$.

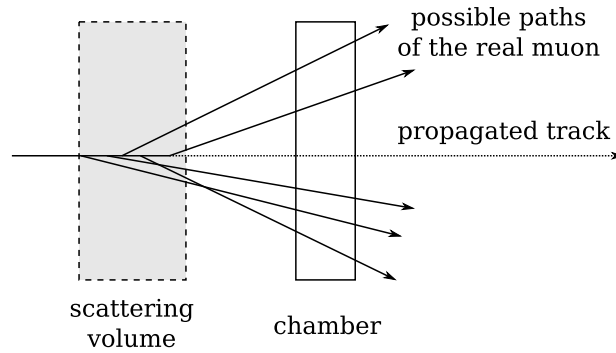


Figure 11: Correlation between super-residual position error and angle error.

there is some evidence that superlayer 2 residuals and station 1, wheels ± 2 are imperfectly represented.

Table 12 summarizes the fits and alignment parameters for each chamber.

2.5 Accomodating errors in magnetic field and material budget

Early in commissioning, track propagation through CMS may suffer from poor knowledge of the magnetic field map and material budget. This would result in incorrect residuals and potentially a wrong alignment. Since alignment is itself a commissioning task, it must be made independent of any propagation errors. Magnetic field and dE/dx errors from an incorrect material budget can be identified by their distinctive dependencies on momentum, and can both be cancelled by taking advantage of the fact that they affect residuals in a charge-antisymmetric way.

Fig 13 derives the effect of B_z (axial) errors on super-residuals, which is proportional to q/p_T but not a simple function of the actual ΔB_z error. A similar derivation would reveal that residuals from B_r (radial) errors are proportional to q/p_z (Fig 14).

As an aside, note that the dependence of super-residuals slopes such as ϕ_y on q/p_T and q/p_z is also bilinear, but easier to interpret as measureable errors in the ΔB_z and ΔB_r components (Fig 15). This is because the cumulative effect that \vec{B} errors have on the angle of a track is simply the integral over its path, while the effect on residuals is a double-integral. Magnetic field errors can therefore be measured directly with tracks, using an extension of the ϕ_y chamber angle measurement.

Residuals from dE/dx errors have a different momentum dependence, but the same dependence on charge. In the momentum range of interest, the energy muons lose in material is independent of momentum: about 2 MeV cm²/g, or 1.6 GeV/m through iron. The track propagator accounts for known material, so only errors in the material budget contribute to residuals. Energy loss affects all three components of the track's momentum equally, so the θ angle of the track's trajectory ($\tan \theta = p_T/p_z$) is unchanged. The Δx and $\Delta \phi$ super-residuals scale in the following ways:

$$\Delta x \propto \ell^2 q B_z \left(\frac{1}{p_T} - \frac{1}{p_T - \cos \theta dE/dx} \right) \quad (9)$$

$$\Delta \phi \propto \ell q B_z \left(\frac{1}{p_T} - \frac{1}{p_T - \cos \theta dE/dx} \right). \quad (10)$$

which is approximately quadratic:

$$\frac{\frac{1}{p_1} - \frac{1}{p_1 - \Delta}}{\frac{1}{p_2} - \frac{1}{p_2 - \Delta}} = \frac{p_2}{p_1} \frac{1 - \left(1 - \frac{\Delta}{p_1}\right)^{-1}}{1 - \left(1 - \frac{\Delta}{p_2}\right)^{-1}} \approx \frac{p_2}{p_1} \frac{1 - \left(1 + \frac{\Delta}{p_1}\right)}{1 - \left(1 + \frac{\Delta}{p_2}\right)} = \left(\frac{p_2}{p_1}\right)^2 \quad (11)$$

In principle, we could determine alignment corrections, magnetic field errors, and dE/dx errors all at once by adding linear and quadratic terms to our fit function. However, that would unnecessarily reduce the statistical precision of our alignment measurement, especially if propagation errors are small. Instead, we note that both types of propagation errors are

Fits to DT superlayers 1 and 3 super-residuals

fit to Δx residuals	fit to ϕ_y residuals
δx : peak of the distribution, independent of impact δz : dependence of the peak on dx/dz track angle ϕ_z : dependence of the peak on y impact point σ, Γ : width of the distribution slope of Δx vs. ϕ_y : model scattering	ϕ_y peak of the distribution σ, Γ : width of the distribution

Fits to DT superlayer 2 super-residuals

fit to Δy residuals	fit to ϕ_x residuals
δy : peak of the distribution, independent of impact ϕ_z : dependence of the peak on x impact point σ, Γ : width of the distribution slope of Δy vs. ϕ_x : model scattering	ϕ_x peak of the distribution σ, Γ : width of the distribution

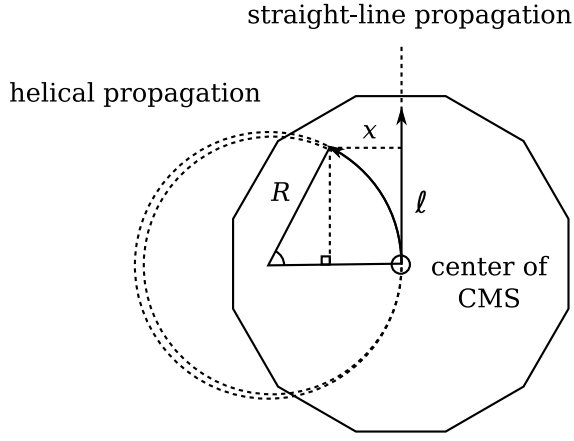
Fits to CSC super-residuals

fit to $\Delta r\phi$ residuals	fit to ϕ_y residuals
$r\delta\phi$: peak of the distribution, independent of impact δz : dependence of the peak on $d(r\phi)/dz$ track angle ϕ_z : dependence of the peak on y impact point σ, Γ : width of the distribution slope of Δx vs. ϕ_y : model scattering	ϕ_y peak of the distribution σ, Γ : width of the distribution

Accessible parameters

	δ_x	δ_y	δ_z	ϕ_x	ϕ_y	ϕ_z (two ways)
DT						
CSC	δ_x	inaccessible	δ_z	inaccessible	ϕ_y	ϕ_z

Figure 12: The six independent fits needed to align one DT chamber and one CSC.



(a) Diagram for derivation: x is the displacement between straight and helical propagation of a track with radius of curvature R at a distance ℓ from the interaction point. If the field is mis-modelled, it would contribute $\Delta x = x_{\text{track}} - x_{\text{muon}}$ to the residual, the difference of two helical propagations with different radii.

Displacement from straight propagation:

$$x = R (1 - \cos(\sin^{-1}(\ell/R)))$$

$$x \approx R \left(\frac{1}{2} (\ell/R)^2 \right) = \frac{\ell^2}{2R}$$

Relationship to magnetic field B_z :

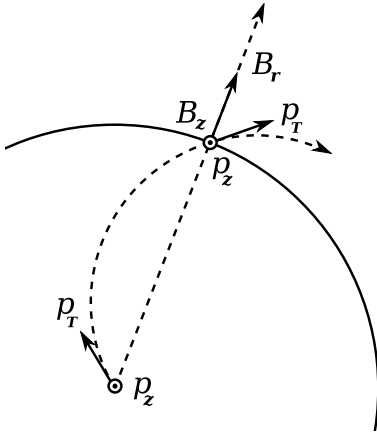
$$R = \frac{\ell^2}{2x} = 300 \text{ cm T/GeV} \frac{p_T}{qB_z}$$

Residuals from field error ΔB_z :

$$\Delta x = \frac{\ell^2}{2 \cdot 300 \text{ cm T/GeV}} \left(\frac{q}{p_T} \right) \Delta B_z$$

(b) Derivation of residuals dependence on q/p_T if the magnetic field is mis-modelled. If the B_z error is also non-uniform, the above holds with “ ΔB_z ” being a (non-trivial) quantity derived from field error along the track’s path.

Figure 13: If the z component of the magnetic field is poorly understood at the time of alignment, the error it contributes to residuals would be proportional to q/p_T .



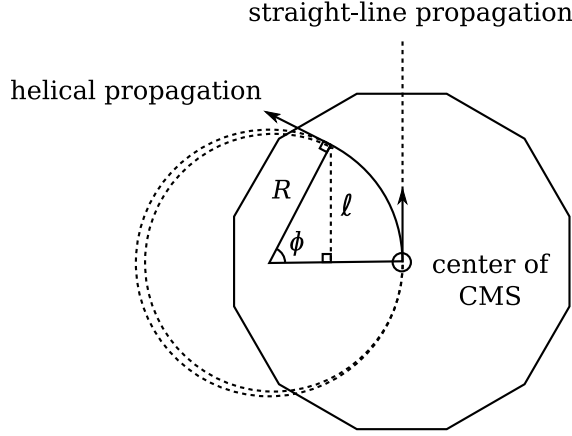
Components affecting $r\phi$ and ϕ_y residuals:

- $|\vec{p}_T \times \vec{B}_z| = |\vec{p}_T| |\vec{B}_z|$, always normal to trajectory
- $|\vec{p}_z \times \vec{B}_r| = |\vec{p}_z| |\vec{B}_r|$, approximately normal to trajectory at high momentum

Components affecting z and ϕ_x residuals:

- $p_T \times B_r$, negligible at high momentum

Figure 14: A summary of magnetic field components which affect residuals.



(a) Track angles are deflected $\phi = \sin^{-1} \ell/R \approx \ell/R$ relative to a straight-line propagation. If the magnetic field is mis-modelled, it would add $\Delta\phi = \phi_{\text{track}} - \phi_{\text{muon}}$ to the super-residual slope.

$$R = \frac{\ell}{\phi} = 300 \text{ cm T/GeV} \frac{p_T}{qB_z}$$

$$\Delta\phi = \frac{\ell}{300 \text{ cm T/GeV}} \left(\frac{q}{p_T} \right) \Delta B_z$$

(b) Derivation of super-residual angle in the presence of mis-modelled B_z . If non-uniform, “ ΔB_z ” is a simple average of magnetic field error along the track’s path.

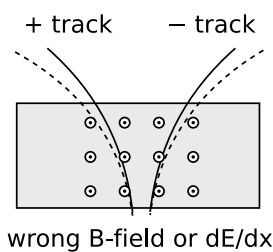
Figure 15: Magnetic field errors would also affect super-residual slopes.

antisymmetric with charge: positive and negative tracks would be deflected in opposite directions (opposite sign in the residuals contribution) by either effect (Fig 16(a)). If we compute all of our alignment corrections from positively-charged tracks and again with negatively-charged tracks, the charge-antisymmetric effects would cancel in the average (Fig 16(b)), assuming that the positive and negative muons have the same momentum distributions (Fig 16(c)). We therefore apply the following “two-bin” method to calculate all alignment constants:

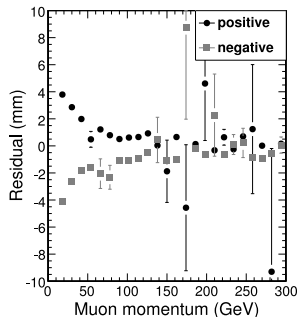
1. Separate the data into two bins by charge.
2. Compute all alignment corrections for each bin separately (R_+ and R_-).
3. Average the two to obtain final alignment results: $\frac{R_+ + R_-}{2}$.
4. Compute a maximally-affected quantity to trace the errors: $\frac{R_+ - R_-}{2}$.

The systematic error after applying this procedure is a small fraction of the error tracer; its exact value depends on how many muons are placed in the wrong bin due to charge confusion and the degree to which the shapes of the spectra differ for the two charges. This quantity is also useful for finding problematic regions of the detector.

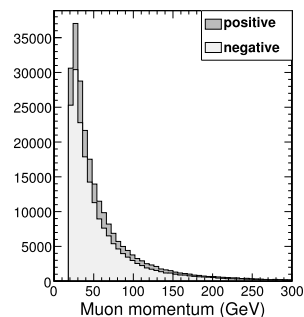
Positive and negative cosmic rays are known to have proportional spectra in our momentum range of interest: the charge ratio of cosmic secondaries is flat as a function of momentum. Most collisions muons should also have this property, as b and \bar{b} are produced in equal abundance. Muons from W bosons may be asymmetric because W^+ and W^- are produced with different rates in pp colliders, but it is likely that the \vec{B} and dE/dx issues



(a) Both \vec{B} and dE/dx errors affect positive and negative muons in opposite ways.



(b) The two effects depend on momentum, but are still antisymmetric for charges in a given momentum bin.



(c) The momentum spectra for the two charges are proportional (cosmic rays shown above).

Figure 16: The two-bin method for cancelling \vec{B} and dE/dx errors: compute corrections separately for positive muons and negative muons, then average the two results.

will be resolved before we're fortunate enough to enrich our muon sample with W decays (by raising the p_T cut).

Fig 17 demonstrates the robustness of the two-bin method in cosmic rays: a correction in the magnetic field map adjusts error tracer values, but not alignment residuals from the averaging technique.

3 Monitoring Tools and Validation/Verification

Visual monitoring of the alignment procedure is useful for two purposes: validation and verification. By “validation,” we mean simply checking that the procedure is valid, that it centers residuals distributions as intended. We will reserve the word “verification” for measurements that independently determine whether the aligned chamber positions accord with reality. If, for instance, tracks are distorted by a systematic effect other than alignment, validation procedures would pass, because they, too, are affected, but verification procedures would not.

A generic example of validation would be to simply run the alignment procedure twice with the same tracks: if the second alignment yields zero corrections, then it validates the first alignment. One way to actually verify the aligned positions would be to select three tracking volumes, A , B , and C , where A is used as a reference to align B and C , then B is used as a reference to align C with a different distribution of tracks. If the two procedures agree about the position of C , then C 's result has been independently verified as a real position in space.

Verification procedures do not need to be completely independent to be useful. As long as they contain some new information that is systematically distinct from the alignment procedure itself, they can add confidence to the measurement. Monitorable quantities range from pure validation to pure verification, and it will be important to keep in mind roughly how much new information each observable is giving us.

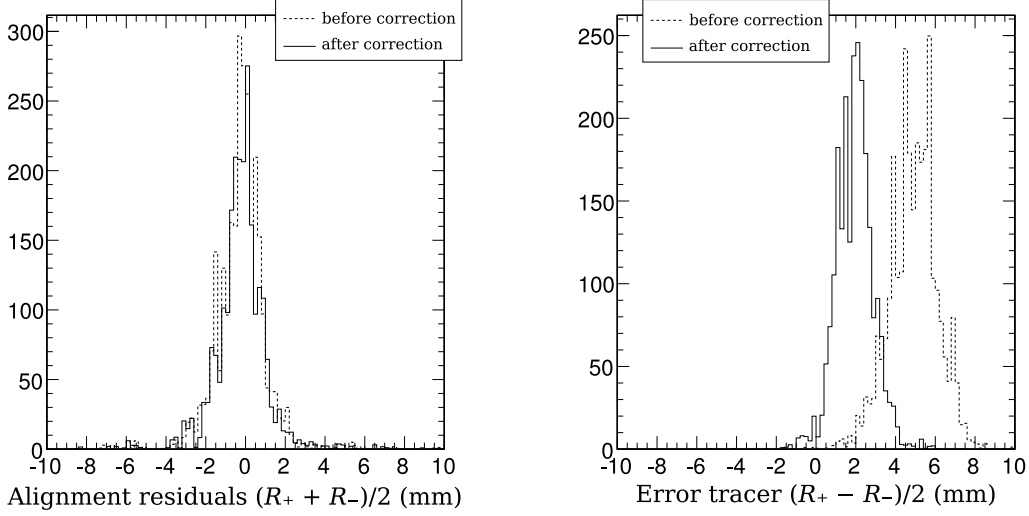


Figure 17: Alignment residuals and the error tracer before and after a correction to the magnetic field map (in DT station 4 with cosmic rays). The alignment residuals are unaffected by the large change in magnetic field values (20–30%).

This section will focus on monitoring methods and show example plots, created under different circumstances, not necessarily the final alignment. For summary plots of alignment results, see sections 4 and 5. We only show a representative subsample of the detailed plots (which are by necessity numerous), while the summary plots contain the complete results.

3.1 Comparison of geometries in the database

Our first validation tool merely checks to see if geometry descriptions in the conditions database differ, and by how much. It is actually a program which converts database records into human-readable XML files and a library for plotting geometrically relevant differences in pyROOT. The conversion can be reversed: the same XML descriptions can be uploaded to the database as muon alignments for track-reconstruction. The features of this system are all documented on its own twiki page: SWGuideMuonGeometryConversion [4].

In this note, we use the conversion tool to prepare test-pattern and randomized misalignment scenarios for the Monte Carlo study, and to plot differences in chamber parameters with respect to ideal.

3.2 Validating residuals fits

Our alignment fits are multi-parameter over a multi-dimensional space, which is in principle dangerous. The fitter has a large space in which to find an unphysical minimum, and multi-dimensional data is hard to visualize quantitatively. However, our fit function has a shape that can easily be unfolded and plotted on a 2-dimensional page. The full fit function is a bell curve (Eqn 4) with the peak (x_0) being a multi-linear function of several variables: δ_x (constant), ϕ_z (slope with respect to position y), δ_z (slope with respect to entrance angle dx/dz), and a control parameter for scattering (slope with respect to super-residual slopes

$\Delta\phi_y$). The multi-linear part can be regarded as a set of corrections to the peak position, which follows a line in $(y, dx/dz, \Delta\phi_y)$ space, like the crest of a mountain ridge.

To best understand the shape of the bell curve, we plot the residuals distribution with y , dx/dz , and $\Delta\phi_y$ corrections applied to the data. The fit width parameters σ and Γ apply to this corrected curve. We also overlay the raw distribution, which is in general wider, but usually not visibly so. (The residuals distribution is much wider than any of the three peak corrections.) Plots like this are in the first column of Fig 18.

To validate the control parameters, we draw profile plots of residuals versus each dimension separately, with all corrections applied to the data except the one shown. For example, the ϕ_z correction (second column in Fig 18) is shown as residuals versus y , with dx/dz and $\Delta\phi_y$ corrections applied to the data. The superimposed fit line is simply $f(y) = \delta_x + \phi_z y$, the crest of the bell-curve extruded in y . As explained in section 2.4, some parameters do not have enough sensitivity to yield a good fit, so they have been fixed. They are still plotted, and thus they appear as horizontal lines.

We control for magnetic field and dE/dx errors by performing the fit separately on positively-charged and negatively-charged muons, and averaging the results. The μ^+ fits are shown in the top row of plots in Fig 18, while the μ^- fits are in the bottom row. A vertical line through the bell curve shows the average, so if track propagation is affected by an error which is antisymmetric in charge, the two bell curves would move away from the vertical line in opposite directions.

It is possible to visually inspect hundreds of fit functions on a computer screen, but more difficult to peruse them in published form. We therefore treat these as diagnostic plots, scanning through them in early alignments for safety and producing them on demand for suspicious fits. In all of the Monte Carlo and real-data alignments observed so far (thousands), the only fits which can be said to not represent the distributions are the ones with very few entries (fewer than ~ 50).

3.3 Muon system maps

The fit-validation plots presented trends in residuals distributions inside each chamber. These trends were expected because they are caused by misalignments. However, if there are unexpected biases in the tracks used for alignment, either due to tracker misalignments or propagation errors, they would show up as trends in the residuals that cross chamber boundaries. To verify our expectation that residuals are correlated within each chamber and uncorrelated outside, we plot maps of the residuals across the whole muon system.

The measurement planes of the DT chambers lie nearly flat in ϕ and z , so these are the relevant abscissas for the map plots. To make sure that no more than one chamber corresponds to each bin in the plots, the plots versus z must be split by sector, the plots versus ϕ must be split by wheel, and all plots must be split by station. The endcaps have 18 rings which are one CSC thick (counting ME1/1a as being distinct from ME1/1b), so each of these gets a separate ϕ plot. The CSCs lie flat in ϕ and the radial direction, instead of z , so the orthogonal plots are 36 radial spokes for each of the 8 disks. Some examples are shown in Fig 19.

On each of these axes, we plot all 6 alignment results: δ_x , δ_y , δ_z , ϕ_x , ϕ_y , and ϕ_z , as well as the antisymmetric combination of fit results to trace $\vec{B}(\vec{x})$ and dE/dx errors. Every

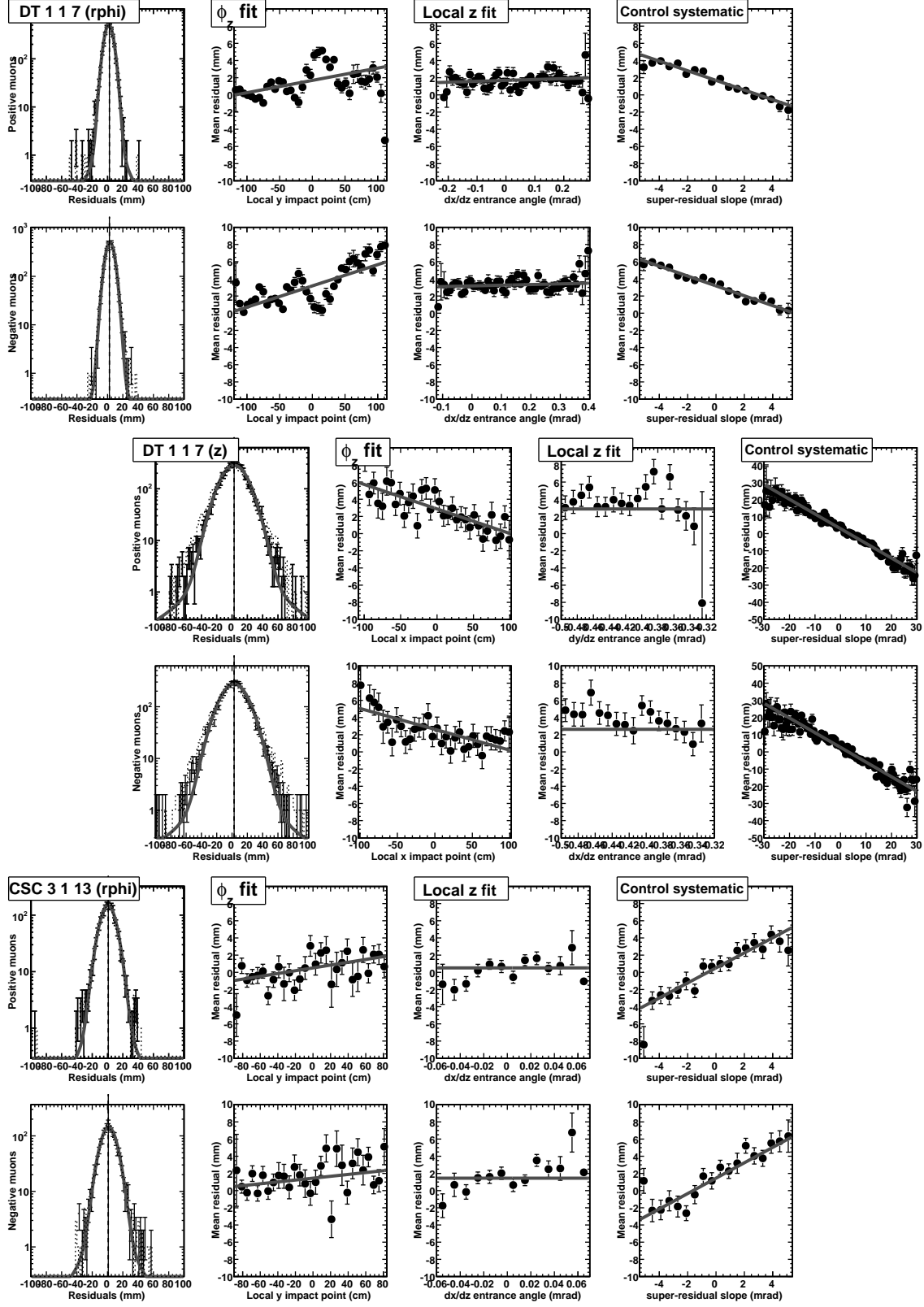


Figure 18: Residuals fits for DT superlayers 1 and 3 (top), DT superlayer 2 (middle), and CSCs (bottom), from Monte Carlo with random misalignment. See text for a full description.

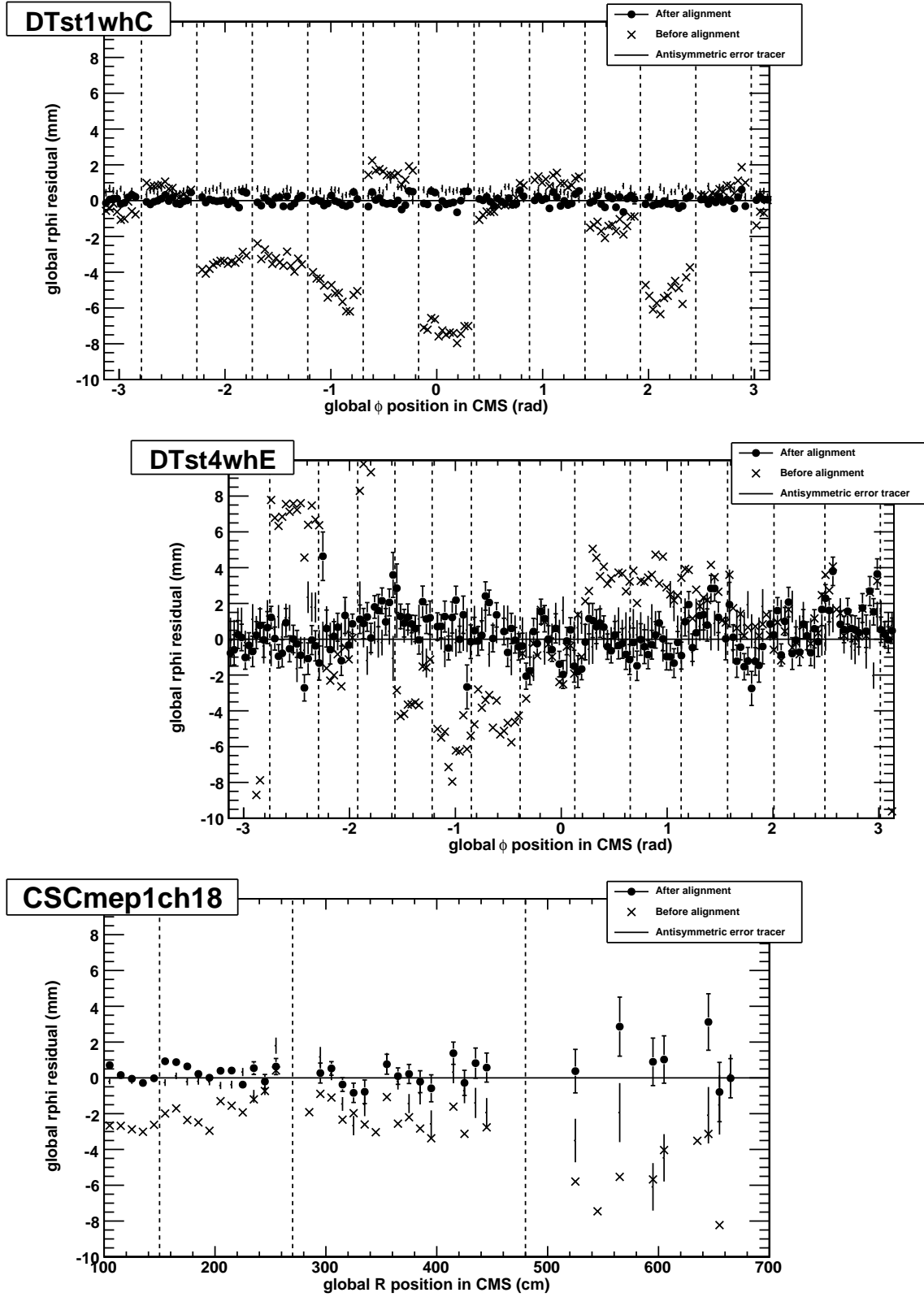


Figure 19: Three maps of residuals before and after alignment in Monte Carlo: DT station 1, wheel 0 (top), station 4 wheel +2 (middle), and CSC ME+1, chamber 18 (bottom). Chamber identities were not used to make the plots; boundaries are overlaid on the results.

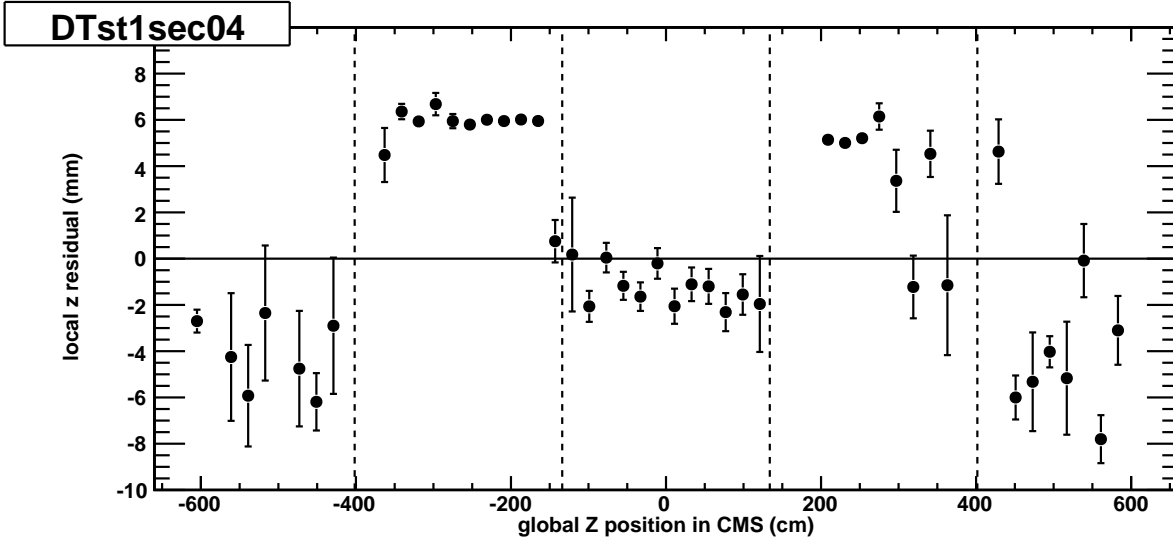


Figure 20: Results of δ_z fits (radial alignment for DT chambers) as a function of global z position. Results agree within each chamber and disagree with their neighbors, indicating real radial misalignments.

bin is derived from the full fitting procedure described in section 2.4, though parameters equivalent to the binning are fixed. (Letting the slope of residuals versus x float in a dataset representing a narrow slice in x would statistically weaken all of the fit's results.) As with the fit-validation, there are too many plots to publish, but they are useful for diagnostics. An example of DT δ_z (radial displacement) in cosmic ray data is presented in Fig 20. This is a complicated quantity, the slope of fits to residuals versus track entrance angle, and it shows clear discontinuities at the chamber boundaries, indicating a real misalignment.

The muon system maps are the basis for binned-residual summary plots, where the points in the maps are used to fill a histogram, and therefore present all of the data on one page (trading depth for breadth). Such a plot is more incisive than a simple histogram of residuals, because pre-averaging the residuals in geographically relevant bins highlights systematic deviations from zero, rather than hiding it under track-by-track scattering. The width of the binned-residual distribution depends on the size of the bins, but they are standardized: 180 bins in ϕ from $-\pi$ to π , 60 bins in z from -660 cm to 660 cm (for DTs), and 60 bins in radial position, from 100 cm to 700 cm (for CSCs). Fig 17 from section 2.5 presented histograms of residuals binned in z .

3.4 Verification with relative residuals

The map plots provide some verification of the alignment in that they meaningfully compare residuals from the same chamber with residuals from neighboring chambers, and thus distinguish between distortions related to the chamber and distortions related to the tracks. However, they are the same residuals that were used to perform the alignment, and are therefore not independent.

Independent sets of residuals allow us to more fully verify the alignment by triangulation:

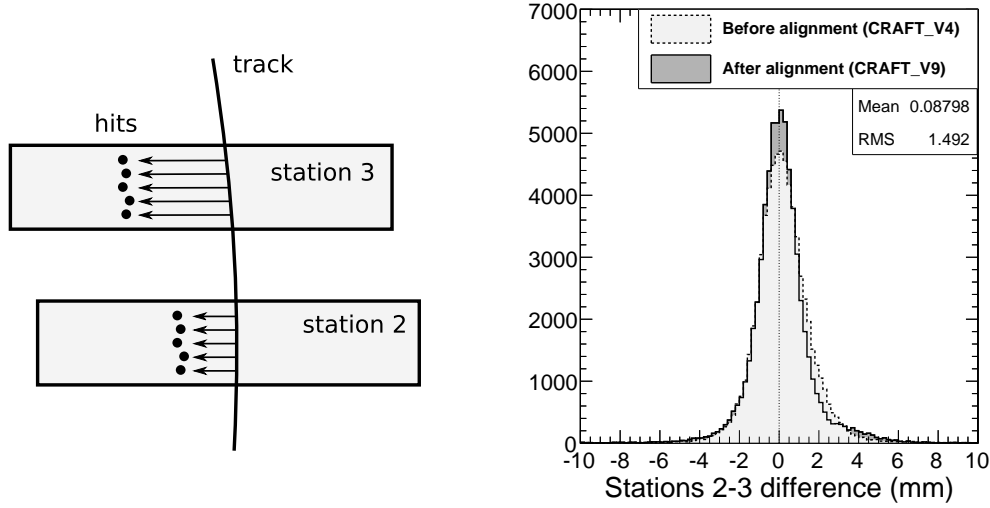


Figure 21: Relative residuals are linearly independent from the residuals used in alignment, and can therefore verify its correctness. PLACEHOLDER! This plot is from the old (3-parameter) CRAFT alignment. AND it's the only one that showed (marginal) improvement—stations 1–2 and 3–4 showed (marginal) degradation. (We interpret the three as indicating no net change in *relative* positions.) In the new plot, we'll combine all stations, since they have comparable widths.

after having aligned each chamber individually to the tracker, we check the alignment with residuals on tracks connecting the chambers themselves. One way to do this re-uses the alignment tracks, but ignores position information from the tracker. Consider the difference of residuals between two stations on each track, diagrammed in Fig 21:

$$\text{residuals difference}(3, 2) = (\text{station 3 track impact point} - \text{station 3 hit position}) - (\text{station 2 track impact point} - \text{station 2 hit position}). \quad (12)$$

The tracker's position information cancels in the residuals difference, as well as any random scattering that happens between the tracker and station 2. The residuals difference is therefore a narrower distribution than absolute residuals and represents the relative alignment of chambers in station 2 and chambers in station 3 (sector by sector). The advantage unique to this method is that the track retains momentum magnitude information from the tracker: it is a curved ruler, where the appropriate curvature is determined by the tracker's high-precision momentum measurement. The difference can be calculated for any pair of neighboring stations, but is difficult to interpret for DT stations 4 and 3, because the sector boundaries in station 4 don't line up with those in station 3.

A more extensive version of the same idea uses a set of aligned chambers as a new reference for track-fitting and re-aligning their neighbors. Chambers aligned by both methods verify the technique, though with less precision because the momentum resolution of the muon system is not as high as the tracker. Without collisions, this is the only way to align some chambers in the muon system, because the constraint requiring cosmic rays to pass through the tracker yields very few tracks in the high $|z|$ regions of the detector.

4 Global alignment results with collisions Monte Carlo

A study of alignment with 50 pb^{-1} of simulated muons from QCD (primarily $b \rightarrow \mu$, which is the majority of the muons that we'll see). I have the event samples in AlCaReco format, so it's ready to go. I've put it on hold until the tracker alignment is sufficiently well understood for us to do a combined alignment study which will become the new 50 and 200 pb^{-1} alignment scenarios.

4.1 Scaling with statistics

4.2 Dependence on tracker misalignment

4.3 Dependence on magnetic field errors

5 Global alignment results with cosmic ray data

I've described all of the method and plotting techniques, so this section will be light on text and heavy on plots with interpretations. I'm running the alignment now, and re-running it with small changes in the configuration to optimize our use of the data. I'll make all of the plots when I have a final alignment, ready to be used for tracker-pointing re-processing.

5.1 Validation plots

5.2 Verification with relative residuals

5.3 Verification with stand-alone muon alignments

This will take several weeks longer than everything else.

5.4 Verification with cosmic track splitting

Cosmic track splitting study by Nhan Tran and Alessio Bonato applied to global muons. It's independent because nothing in the alignment procedure explicitly correlated the top chambers with the bottom chambers. It will need to be repeated with the new alignment (as well as the new magnetic field, new tracker alignment, and new tracker weights). Naturally, they'll need to be acknowledged.

6 Relative alignment of CSCs with local tracks

We have focused so far on global alignment because of its importance in muon track-fitting, but local alignment methods have a different set of advantages which can be used to improve our overall understanding. Locally-propagated tracks, for instance from one chamber to its neighbor, suffer far less from propagation errors, yielding narrower residuals distributions and fewer systematic uncertainties. High precision can be achieved with fewer tracks because of the narrowness of the residuals, and the track source need not point to the tracker, so the

endcap can be aligned before first collisions with beam-halo data. When collisions muons are available for the global alignment procedure, local alignment will severely test it and provide diagnostics in the case of a disagreement.

The disadvantage of local alignment algorithms is that they do not relate the coordinate frame of the aligned system to a common standard. In this section, we will describe a procedure that aligns CSCs within rings, but does not relate the aligned rings to each other or the tracker. Global muons from collisions will be required to make this connection, though we can combine residuals from all the chambers in each ring to minimize statistical uncertainty and average over possible systematic effects.

6.1 Description of the CSC Overlaps algorithm

In the muon endcap, CSCs were designed to overlap slightly with their neighbors for the purpose of local alignment. In each ring except ME1/3, tracks on the left edge of chamber i can be expected to also pass through the right edge of chamber $i + 1$, so both chambers can independently determine the track parameters with all 6 layers. If these chambers systematically disagree about the positions of tracks in a shared coordinate system, then one or both are misaligned. Relative alignment corrections can be propagated through the ring until we return to the first chamber, at which point the collection of chambers must form a consistent circle, a constraint known as closure.

This can be made more formal by defining $N = 18$ or 36 alignment corrections A_i (where $i \in \{1 \dots 18\}$ for ME2/1, ME3/1, ME4/1 and $i \in \{1 \dots 36\}$ for the other stations). The ring also has N residuals distributions, but each residuals distribution corresponds to a pair of chambers, not an individual chamber, because each residual is the position of the track as measured in chamber i minus the position of the track as measured in chamber $i + 1$. (Index arithmetic should be presumed to be mod N , such that $i + 1 = 1$ when $i = N$. Remember that the chambers are arranged in a circle.) To use the language of the preceeding sections in this note, we may think of one chamber as the reference tracking volume and the other as the target to be aligned, except that there is no reason to prefer one as a reference above the others. Label the mean of the residuals distribution corresponding to chambers i and $i + 1$ as $\alpha_{i, i+1}$. We can use the mean of the residuals distribution, rather than a fit for its peak, because scattering is not an issue.

If we move chambers i and $i + 1$ by A_i and A_{i+1} , the mean of the overlap residuals can be expected to change from $\alpha_{i, i+1}$ to $\alpha_{i, i+1} - (A_i - A_{i+1})$. We want to find a complete set of corrections to minimize all of the residuals means, so we define a χ^2 as

$$\chi^2 = (\alpha_{12} - A_1 + A_2)^2 + (\alpha_{23} - A_2 + A_3)^2 + \dots + (\alpha_{N1} - A_N + A_1)^2 \quad (13)$$

and minimize it by setting its derivatives to zero. For example,

$$\frac{1}{2} \frac{\partial \chi^2}{\partial A_2} = (\alpha_{12} - A_1 + A_2) - (\alpha_{23} - A_2 + A_3) = 0. \quad (14)$$

The complete set of such equations, written in matrix form, looks like the following (with

$N = 5$ for brevity):

$$\begin{pmatrix} \alpha_{12} - \alpha_{51} \\ \alpha_{23} - \alpha_{12} \\ \alpha_{34} - \alpha_{23} \\ \alpha_{45} - \alpha_{34} \\ \alpha_{51} - \alpha_{45} \end{pmatrix} = \begin{pmatrix} 2 & -1 & & & -1 \\ -1 & 2 & -1 & & \\ & -1 & 2 & -1 & \\ & & -1 & 2 & -1 \\ -1 & & & -1 & 2 \end{pmatrix} \begin{pmatrix} A_1 \\ A_2 \\ A_3 \\ A_4 \\ A_5 \end{pmatrix}. \quad (15)$$

To align all N chambers, we need only invert this $N \times N$ matrix. We did not break the symmetry between the reference system and the target system: this procedure mutually aligns all chambers at once (similar to the MillePede algorithm used to align the tracker, but a much smaller computational scale: our $N \ll$ millions).

Unfortunately, the matrix in Eqn 15 is singular because a procedure like this cannot determine the global position of the whole system. Adding the same constant to every A_i , which would rotate the whole ring rigidly, would leave the χ^2 invariant because the relative positions of every pair of chambers is unchanged by the collective motion. Since there is a direction in $\{A_i\}$ -space in which χ^2 is flat, it cannot be minimized by setting its derivatives to zero. One way to solve the problem is to refuse motion in the flat direction by fixing one chamber, e.g. force $A_1 = 0$ and make chamber 1 the reference.

$$\begin{pmatrix} 0 \\ \alpha_{23} - \alpha_{12} \\ \alpha_{34} - \alpha_{23} \\ \alpha_{45} - \alpha_{34} \\ \alpha_{51} - \alpha_{45} \end{pmatrix} = \begin{pmatrix} 1 & 0 & 0 & 0 & 0 \\ -1 & 2 & -1 & & \\ & -1 & 2 & -1 & \\ & & -1 & 2 & -1 \\ -1 & & & -1 & 2 \end{pmatrix} \begin{pmatrix} A_1 \\ A_2 \\ A_3 \\ A_4 \\ A_5 \end{pmatrix} \quad (16)$$

However, if chamber 1 is misaligned, it would take the whole ring with it. Ring misalignments can be corrected later with global alignment, but it is best to avoid introducing them. Instead, we can make the flat direction quadratic in χ^2 by preferring $\{A_i\}$ sets that have an average of zero (minimally rotate the ring). This can be accomplished by adding a term like

$$\left[\frac{1}{N} (A_1 + A_2 + \dots + A_N) \right]^2 \quad (17)$$

to the χ^2 . Each derivative equation becomes

$$\frac{1}{2} \frac{\partial \chi^2}{\partial A_i} = (\alpha_{i-1, i} - A_{i-1} + A_i) - (\alpha_{i, i+1} - A_i + A_{i+1}) + \frac{1}{N^2} \sum_{i=1}^N A_i = 0, \quad (18)$$

so the the matrix equation is now

$$\begin{pmatrix} \alpha_{12} - \alpha_{51} \\ \alpha_{23} - \alpha_{12} \\ \alpha_{34} - \alpha_{23} \\ \alpha_{45} - \alpha_{34} \\ \alpha_{51} - \alpha_{45} \end{pmatrix} = \left[\begin{pmatrix} 2 & -1 & & & -1 \\ -1 & 2 & -1 & & \\ & -1 & 2 & -1 & \\ & & -1 & 2 & -1 \\ -1 & & & -1 & 2 \end{pmatrix} + \frac{1}{N^2} \begin{pmatrix} 1 & 1 & 1 & 1 & 1 \\ 1 & 1 & 1 & 1 & 1 \\ 1 & 1 & 1 & 1 & 1 \\ 1 & 1 & 1 & 1 & 1 \\ 1 & 1 & 1 & 1 & 1 \end{pmatrix} \right] \begin{pmatrix} A_1 \\ A_2 \\ A_3 \\ A_4 \\ A_5 \end{pmatrix}. \quad (19)$$

It has a unique solution in which the average correction (Eqn 17) minimized to exactly zero. Actually, adding any non-zero constant to every element would yield the same solution as the physically-motivated $\frac{1}{N^2}$.

The circular ring of chambers also provides an internal cross-check: the sum of the means of pairwise residuals must be zero. If not, no combination of alignment corrections can center all of the residuals, because

$$\text{closure} = \sum_{i=1}^N \alpha_{i, i+1} - (A_i - A_{i+1}) = \sum_{i=1}^N \alpha_{i, i+1} \quad (20)$$

is independent of $\{A_i\}$. (Note that $\sum_{i=1}^N A_{i+1}$ is just a reindexing of $\sum_{i=1}^N A_i$ because index arithmetic is understood to be mod N .) With non-zero closure, the solution of Eqn 19 uniformly distributes residuals so that they all have non-zero means, which is to say, every chamber disagrees with its neighbor about where the tracks are. Unclosed $r\phi$ residuals either imply

- the average distance of the chambers from the beamline is incorrect, or
- the presumed width of the chambers is incorrect.

In the first case, the circumference of the ring is miscalculated because the wrong radius is assumed; in the second case, the wrong arc is assumed per chamber. In the course of developing this technique, we discovered a 15 mm closure error, which derived from an 800 μm error in the active width of the chamber description, ultimately from a 0.09% error in the pitch angle of each cathode strip (10 μm per strip). It is a very sensitive technique!

6.2 Local CSC alignment parameters

As much as possible, the same techniques are used to calculate residuals and alignment corrections in the local procedure as in the global. Tracks propagated to a chamber are compared with the chamber's segment position and angle, much like the super-residuals described in section 2.2. Anode wire measurements are ignored due to their large granularity, and strips are taken to measure curvilinear $r\phi$ residuals, rather than cartesian local x , again in direct analogy with the global procedure. The difference is that the source for global tracks is the tracker, propagated through magnetic fields and many radiation lengths of material, while local tracks are extrapolations from a linear fit in the neighboring chamber. To treat

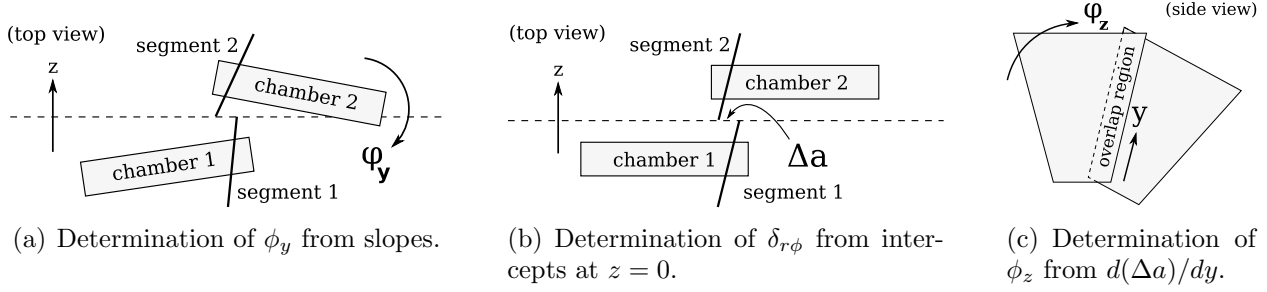


Figure 22: The three alignment parameters accessible to local track matching in CSCs.

the pair of chambers symmetrically, hits in each are fitted to line segments on the surface of a cylinder around the beamline

$$\phi(z) = a + bz \quad (21)$$

and the parameters of these two fits are compared at the plane equidistant between the chamber centers (at $z = (z_1 + z_2)/2$, where z_1 and z_2 are the global z positions of the two chambers).

Three parameters are accessible with this technique (Fig 22):

1. the relative ϕ_y of the two chambers is their average difference in slopes (Δb),
2. the relative $\delta_{r\phi}$ position is the difference in intercepts (Δa), and
3. the relative ϕ_z angle is the difference in intercepts as a function of hit position ($d(\Delta a)/dy$).

These parameters are interdependent in the sense that the $\delta_{r\phi}$ result depends on ϕ_y and the ϕ_z result depends on $\delta_{r\phi}$, but the dependencies are unidirectional. If corrected in the above order, first ϕ_y , then $\delta_{r\phi}$, then ϕ_z , the parameters decouple, avoiding the need for a combined fit.

The formalism developed in section 6.1 can be applied to each parameter separately. First, $\alpha_{i, i+1}$ is defined as $b_i - b_{i+1}$ and A_i as ϕ_{y_i} to align the angles, then $\alpha_{i, i+1}$ becomes $a_i - a_{i+1}$ and A_i becomes $\delta_{r\phi_i}$ to align the positions, and similarly for ϕ_z .

6.3 Specialized trigger and data streams

Only events with muons that thread the narrow overlaps between chambers are useful to this procedure, which is a small fraction of the whole. Beam-halo and collisions muons are equally useful, but they come from different sources (primary datasets) because they're reconstructed differently. We therefore have special triggers and data streams for each case, to avoid losing events to generic prescales.

Four triggers are designed to accept beam-halo events. They are

- HLT_CSCBeamHalo: simply passes L1_SingleMuBeamHalo bit, likely to be prescaled,
- HLT_CSCBeamHaloRing2or3: same but additionally requires reconstructed hits in ME $n/2$ or ME1/3, which are less common and therefore deserve a lower prescale,

- HLT_CSCBeamHaloOverlapsRing1 and Ring2: requires clusters of reconstructed hits in neighboring chambers, consistent with a muon in the overlap region.

Naturally, the two specialized overlaps triggers are essential to the CSC Overlaps procedure; the others are for cross-checks and detector studies which may be unrelated to alignment. To produce one complete $ME_{n/1}$ alignment per day, we would need 0.4 Hz from HLT_CSCBeamHaloOverlapsRing1, and for one $ME_{n/2}$ alignment per day, we would need 0.8 Hz from HLT_CSCBeamHaloOverlapsRing2 (scaling from 2008 exercise).

Events with beam-halo trigger bits are then collected by the MuAlBeamHaloOverlaps AlCaReco stream (similar to MuAlCallIsolatedMu, MuAlGlobalCosmics, and MuAlStandardAloneCosmics, discussed on page 8). MuAlBeamHaloOverlaps has no explicit p_T cut (the momentum of tracks parallel to \vec{B} would not be measured well anyway), with an option to apply a coarse energy cut by requiring the reconstructed track to pass through a given number of stations.

Collisions muons to be used with the CSC Overlaps procedure are collected with the standard single-muon triggers and whatever prescales that implies (in flux at the low end of the momentum scale). They are then delivered to alignment via the MuAlOverlaps stream. As usual, the AlCaReco streams contain only what is needed for alignment: tracks and the hits associated with those tracks, so they use very little disk space for the number of events they contain.

6.4 Results from the 2008 LHC run

On September 10–17, 2008, protons circulated in the LHC tunnel, providing a source of beam-halo muons which we used to test the CSC Overlaps procedure. Three-quarters of the beam-halo events were collected from a 9-minute run on the evening of September 11 (run number 60232; 33,000 HLT_CSCBeamHaloOverlapsRing1 triggers). To guarantee a consistent snapshot of the detector geometry, we select data from this run only. The CSC Overlaps procedure is only meaningful when applied to rings in which all chambers are actively taking data; missing data in any one chamber removes two residuals constraints (e.g. $\alpha_{i-1, i}$ and $\alpha_{i, i+1}$), making Eqn 19 unsolvable. In this run, ME–2/1 and ME–3/1 were the only completely-active rings (the beam was coming from the minus side of CMS, which contributed significantly more muons to the minus endcap). Many of the CSC commissioning problems experienced in 2008 have been fixed in the long shut-down, so we can expect more complete rings in 2009.

The procedure was first applied to beam-halo Monte Carlo with approximately the same number of events but a different azimuthal and radial distribution than the real beam. (The azimuthal and radial distribution of the real beam varied considerably from run to run, more than the difference between our chosen run and the Monte Carlo.) Fig 23 presents the results from a simulated alignment procedure, starting from a standard misaligned geometry (2008 “STARTUP” scenario). The standard deviation of the difference between aligned chamber positions and MC truth quantifies the precision of the technique, though the interpretation is approximate because of the differences in track distribution.

To verify the aligned positions of chambers in real data, we compare the beam-halo results with photogrammetry, an alignment derived from a literal photograph of the detector. Each

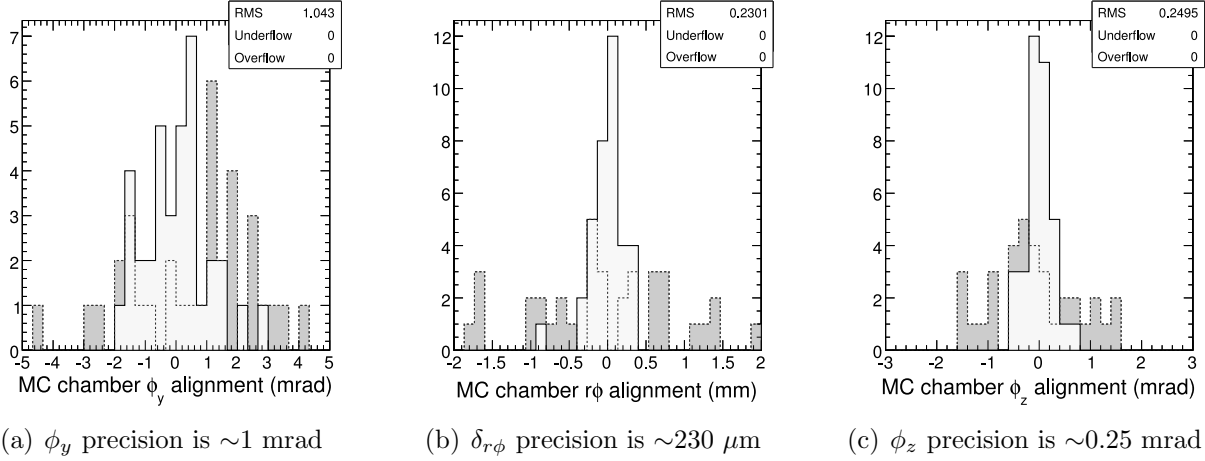


Figure 23: Comparison of alignment parameters with MC truth before (dark) and after (light) a simulated beam-halo alignment with similar statistics to the 2008 LHC run.

chamber has two alignment pins, connected directly to the active layer planes and capped with a reflective disk, the center of which is accurately measured by the photographs. An average of the two pin positions yields the $r\phi$ location of the chamber and a difference of the two pin positions, divided by the distance between the pins, yields the ϕ_z angle. The ϕ_y angle is inaccessible to photogrammetry, because both pins lie on the chamber's local y axis. The photogrammetry results are clearly independent from the track-based results, and can therefore be used to verify the latter. The beam-halo data were collected with no magnetic field, just like the photogrammetry, so we can be confident that they describe the same geometry.

Fig 24 presents the aligned value of each parameter of each chamber relative to ideal values for both track-based alignment and photogrammetry. One can see that the two methods are both measuring significant differences with respect to ideal, and that the results are highly correlated.

To compute the accuracy of the beam-halo alignment with photogrammetry as the reference, we subtract the $\delta_{r\phi}$ and ϕ_z of each beam-halo result from the corresponding photogrammetry result (Fig 25). The mean (bias) is consistent with zero, but in the $\delta_{r\phi}$ case, a non-zero mean would correspond to a global rotation of the disk which is not a measurable parameter in the CSC Overlaps procedure or the single-disk photogrammetry. The standard deviations are 340 μm in $\delta_{r\phi}$ and 0.42 mrad in ϕ_z , which derive from a sum in quadrature of the track-based uncertainties and the photogrammetry uncertainties. Photogrammetry uncertainties are 300 μm for each pin [3], which means $(300 \text{ } \mu\text{m})/\sqrt{2} = 210 \text{ } \mu\text{m}$ for the chamber center position and $(300 \text{ } \mu\text{m}) \cdot \sqrt{2}/1.85 \text{ m} = 0.23 \text{ mrad}$ for the chamber angle. Subtracting the photogrammetry uncertainties in quadrature from standard deviations observed in the plots,

$$\text{track-based } \delta_{r\phi} \text{ accuracy} = \sqrt{(340 \text{ } \mu\text{m})^2 - (210 \text{ } \mu\text{m})^2} = 270 \text{ } \mu\text{m} \quad (22)$$

$$\text{track-based } \phi_z \text{ accuracy} = \sqrt{(0.42 \text{ mrad})^2 - (0.23 \text{ mrad})^2} = 0.35 \text{ mrad} \quad (23)$$

Thus, the 200-300 μm accuracy goals are already demonstrated in a subset of endcap

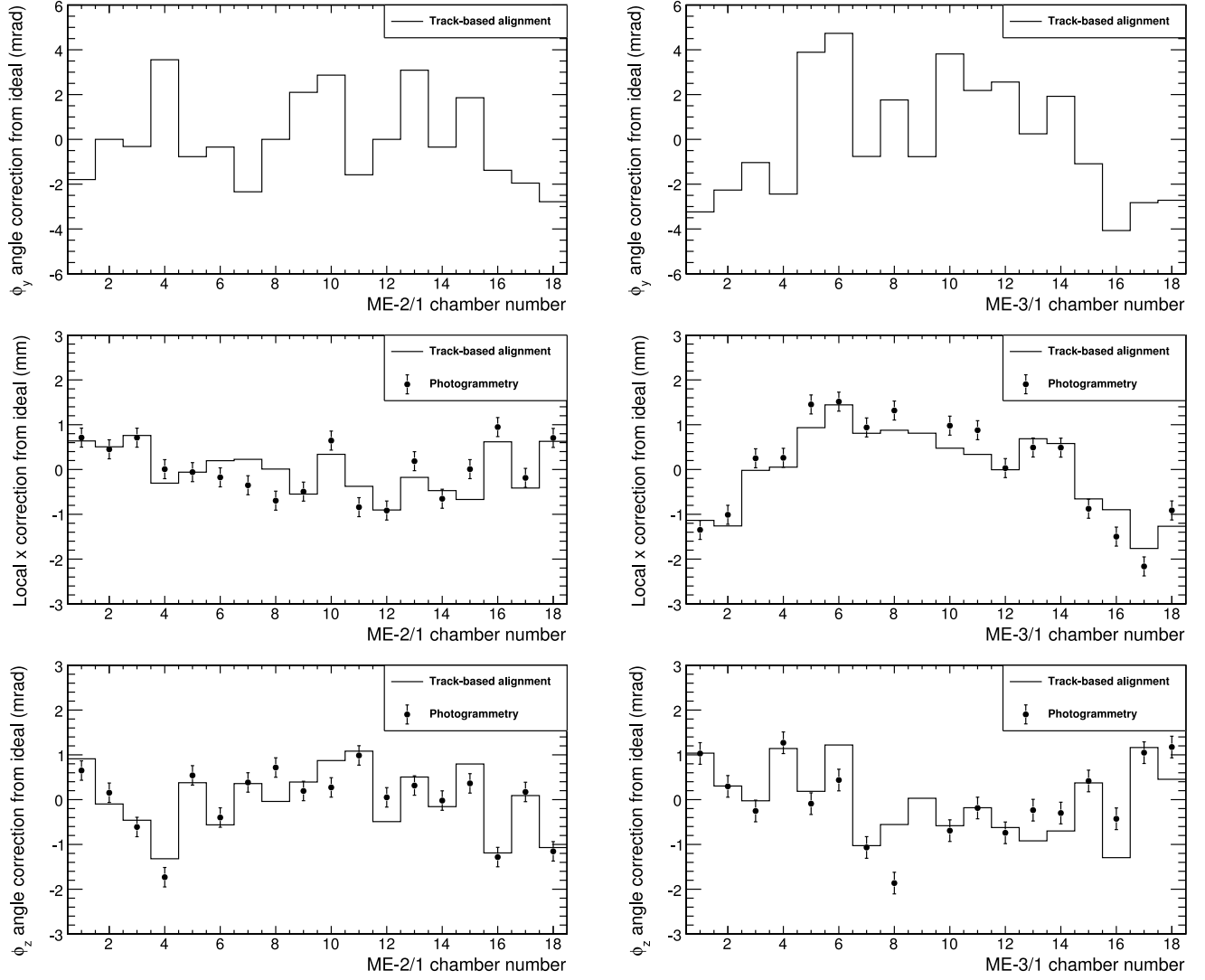


Figure 24: CSC alignment results from the Overlaps procedure and the 2008 LHC run, presented as a difference from ideal and compared with photogrammetry where possible.

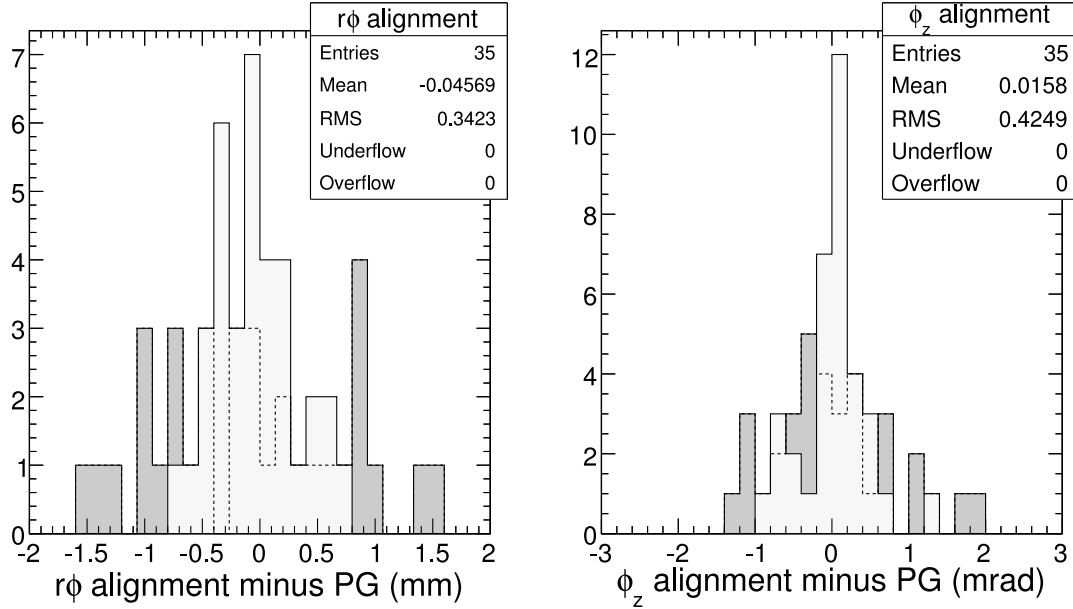


Figure 25: Chamber-by-chamber verification of the beam-halo alignment with photogrammetry. The dark histogram is before alignment; the light histogram and statistics box are after alignment.

chambers, using a local alignment technique. There is no indication that this result is systematically limited; much higher precision may be possible once we collect more than 12 minutes of data.

6.5 Extension to align CSC layers

The CSC Overlaps procedure can be extended to align CSC layers, though the layer procedure only needs to be applied once with high statistics, rather than routinely with a maintainable algorithm. The usual difficulty in aligning layers with local tracks is that the systems are underconstrained. Extra constraints applicable to tracks overlapping well-aligned neighbors allow us to break all of the important degeneracies.

Local alignment procedures require tracks to be fitted locally, which introduces an interdependency between track-fitting and alignment. In the CSC Overlaps procedure, we needed the circular closure constraint to form an overconstrained system, and no such thing is available inside of a chamber. In a chamber, there are 6 layers; in principle, 5 need to be aligned, since the collective position of all the layers is a chamber-alignment issue. But it takes at least 2 parameters to determine each track: one too many. If we simply ignore this fact and constrain the track to two of the layers, we would not know if the layers are skewed like a deck of cards (Fig 26), a plausible misalignment, as it could be caused by a simple tilt of the alignment pins. Small tilts could also escape quality control at the production sites, which measured cathode traces relative to the pins.

A well-aligned pair of neighboring chambers can be treated as a single, 12-layer chamber for tracks that pass through the overlap region. Once misalignments between the two

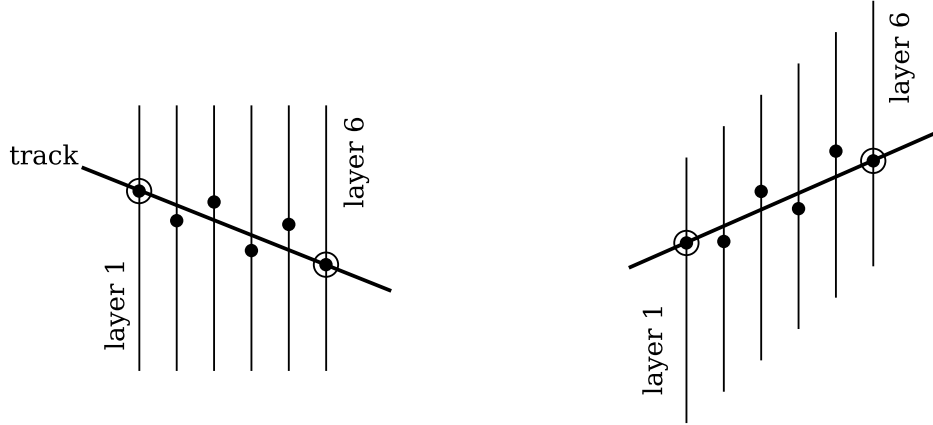


Figure 26: Even when a track is constrained to two only layers, the positions of the other layers can only be determined up to a collective offset and a collective skew. The two situations depicted here are indistinguishable.

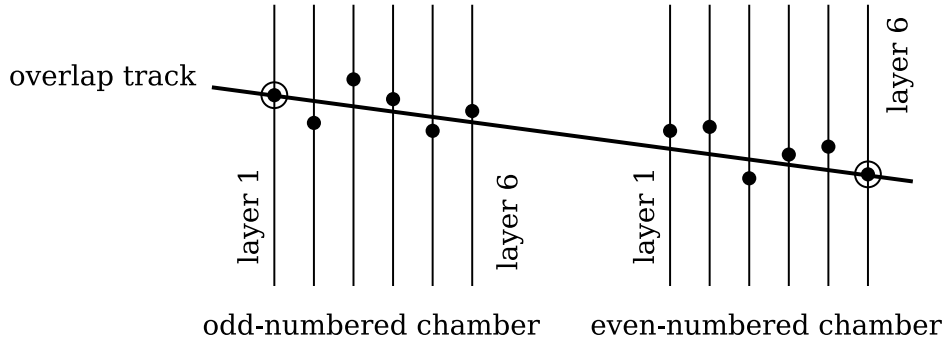


Figure 27: Method for aligning layers within chambers: constrain a linear track to the first and last layers in a two-chamber overlap, then align the remaining layers to that track.

chambers have been corrected with the CSC Overlaps procedure, we can justifiably assume that the 12-layer system is not collectively skewed, and align 10 of the layers to a track constrained to 2 layers (or an equivalent average that maintains the same number of degrees of freedom). Such a procedure is illustrated in Fig 27.

Using beam-halo data from 2008, we applied the above procedure to measure layer corrections in ME-2/1 and ME-3/1. The corrections are generally smaller than $200\ \mu\text{m}$, though some are statistics-limited, due to the azimuthal asymmetry of the beam-halo. They are plotted in Fig 28.

6.6 Verifying the global procedure with local alignment

In addition to providing a nearly-complete alignment of the muon endcaps before first collisions, the CSC Overlaps procedure will diagnose the global alignment procedure. Once collisions muons have been collected in sufficient quantity, we will attempt to align the CSCs

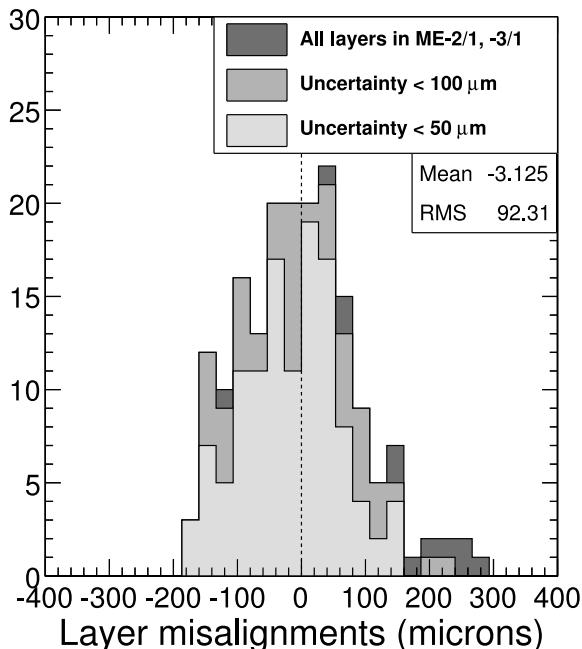


Figure 28: Layer alignment results in ME-2/1 and -3/1, excluding layers fixed by definition.

with global tracks, then check it against the locally-measured result. If the global alignment is correct, it should reproduce the local results, though possibly with lower precision and an overall ring displacement, unobserved by the local measurement.

As previously stated, local track-fitting does not suffer from potential propagation errors, and it is completely independent of any tracker misalignments. Overlaps tracks are a minority, so they can be explicitly excluded from the global alignment procedure for perfect independence. It's also worth noting that the direction in which the CSC Overlaps procedure correlates results, among chambers in the same station, is orthogonal to the way global alignment correlates results, among equal-numbered chambers in different stations. If the global procedure independently aligns chamber i and $i + 1$ to the correct relative values, that would be a strong confirmation.

The local alignment procedure provides a link between the global procedure and photogrammetry. Photogrammetry must be performed when the magnetic field is off and disks are unbent. The global alignment procedure must be performed with the magnetic field on to apply an essential p_T cut; modifications of the global procedure without a p_T cut determined by track curvature would make the comparison less meaningful. Comparing the two is complicated by the fact that the geometry changes when the field is turned on. Local alignment procedures, however, can be performed with or without the magnetic field, because local tracks are approximately linear in either case. We have verified that the CSC Overlaps procedure reproduces photogrammetry with no field; what remains is to verify that the global alignment procedure reproduces the CSC Overlaps.

If there is a discrepancy between local and global alignment results, the similarities

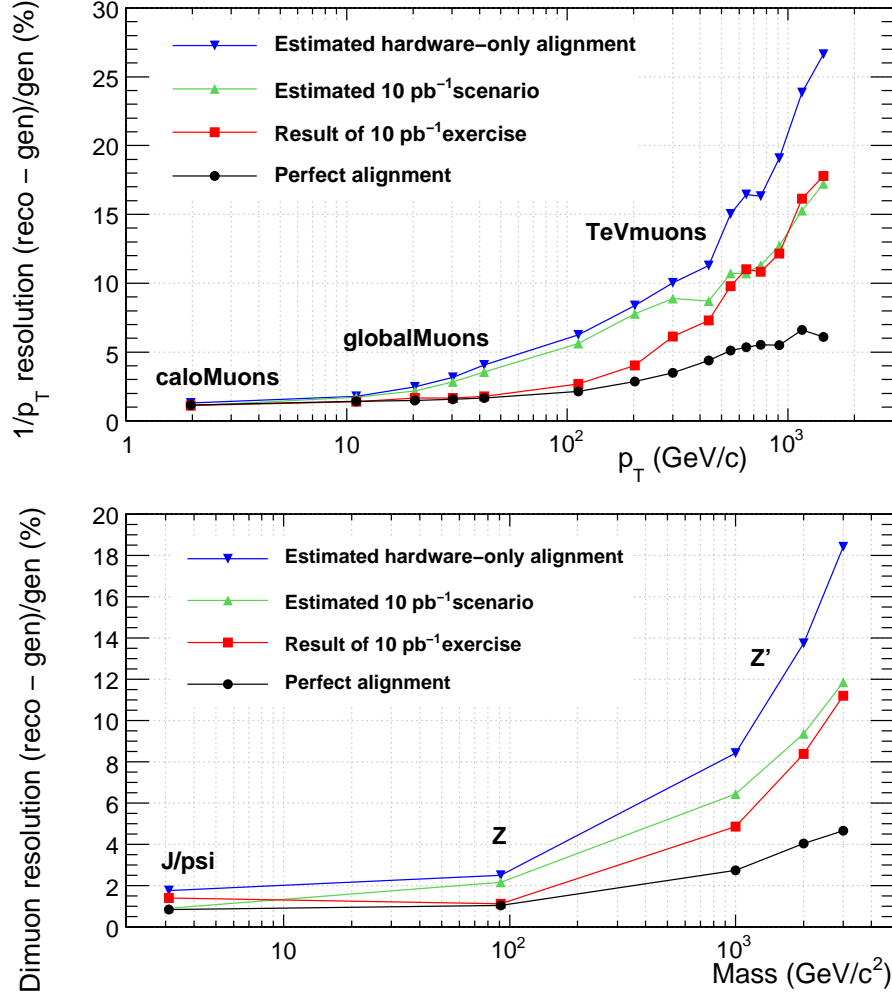


Figure 29: PLACEHOLDER! Track and mass resolutions with 2008-STARTUP, 50, 200 pb^{-1} , and ideal scenarios from the new MC studies.

between the methods suggest follow-up studies. For instance, some tracks pass through both the tracker and the overlap region of a CSC. We could fit the same track both ways and look for discrepancies on a track-by-track basis. Studies such as these would not be possible to diagnose differences between track-based alignment and photogrammetry or a hardware-based alignment.

7 Alignment outlook for 2009–2010

This is where I will review the steps toward alignment in 2009 and present track resolutions from the 50 and 200 pb^{-1} scenarios derived from the “MC Results” section. It will be a schedule of future tasks, a summary of the paper, and a reference for what this alignment means for physics (Fig 29).

References

- [1] TDR
- [2] internal DT reference
- [3] photogrammetry
- [4] <https://twiki.cern.ch/twiki/bin/view/CMS/SWGuideMuonGeometryConversion>